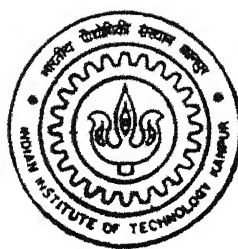


# A COMPRESSIBLE NAVIER-STOKES SOLVER FOR LES

by  
INDRADEEP GHOSH

TH  
ME/2001/M  
G346C



DEPARTMENT OF MECHANICAL ENGINEERING  
INDIAN INSTITUTE OF TECHNOLOGY, KANPUR  
February, 2001

# A COMPRESSIBLE NAVIER-STOKES SOLVER FOR LES

A Thesis Submitted  
in Partial Fulfillment of the requirements  
for the Degree of  
**MASTER OF TECHNOLOGY**

By  
**INDRADEEP GHOSH**



To the  
**DEPARTMENT OF MECHANICAL ENGINEERING**  
**INDIAN INSTITUTE OF TECHNOLOGY, KANPUR**  
**Feb, 2001**

133643



A133643

**Dedicated to my beloved Parents and Sister**

## Certificate

It is to certify that the thesis entitled "A COMPRESSIBLE NAVIER-STOKES SOLVER FOR LES" by Mr. Indradeep Ghosh has been carried out under my supervision. The contents of this thesis have not been submitted to any other Institute or University for the award of any degree and diploma.



(Dr. Subrata Sarkar)  
Assistant Professor,  
Department of Mechanical Engineering,  
Indian Institute of Technology,  
Kanpur - 208016

22 February, 2001

## ACKNOWLEDGEMENT

I am very grateful to my thesis supervisor, Dr Subrata Sarkar for his invaluable guidance, help and inspiration throughout my M Tech program. This work would have been impossible without his presence and guidance. An M Tech program is very complicated but he made it look all that simple and enjoyable and challenging to me with his untiring cooperation, warm heart, everlasting inspiration and encouragement. I am indebted to him forever.

I want to thank ERCOFTAC for providing the experimental dataset to me necessary for validation of the numerical results over a backward facing step.

I am grateful to my friends Arindam and Sudiptada for his untiring cooperation, help and inspiration. The academic discussion I had with during the development of this work helped me a lot.

A lot of smiling faces, especially those of Shamik, Pradipta, Kaushik, Srestha, Subhankar will remain in my memory, which provided me pleasant companion during my stay in IIT Kanpur.

Finally, the blessing and good-wishes of my parents helped me to overcome all the hurdles. I am greatly indebted to them for their constant encouragement and emotional support provided throughout my M Tech program.

## CONTENTS

<b>ABSTRACT</b>	1
<b>NOMENCLATURE</b>	111
<b>LIST OF FIGURES</b>	v
<b>CHAPTER – 1</b>	
<b>INTRODUCTION</b>	1
<b>CHAPTER – 2</b>	
<b>LITERATURE REVIEW</b>	4
2 1 Upwind schemes	4
2 2 LES computations	7
2 2 1 Filtering approach	8
2 2 2 Modelling of SGS terms	8
2 2 3 Scale similarity and mixed model	9
2 2 4 Dynamic SGS modelling	9
2 2 5 SGS for compressible flow	11
2 3 Conclusions	12
<b>CHAPTER – 3</b>	
<b>GOVERNING EQUATIONS AND NUMERICAL SCHEME</b>	13
3 1 Introduction	13
3 2 Governing Equations and LES Model	13
3 2 1 Flow Equations	13

3 2 2 Governing equations for LES	14
3 2 3 Subgrid Scale Model	15
3 3 Numerical Scheme	17
• Calculation of convective fluxes	18
• Calculation of Viscous Derivatives	22
• Time-Integration	24
• Acceleration Techniques	25
Local Time Stepping	25
Residual Smoothing	26
3 4 Closure	27

## **CHAPTER 4**

<b>RESULTS AND DISCUSSION</b>	28
4 1 Introduction	28
4 2 The Euler and Navier-Stokes analyses of flow over a 4% thick circular arc bump	28
4 2 1 Grid generation and boundary conditions	28
4 2 2 Results from the Euler and Navier-Stokes calculations	29
4 2 3 Conclusions	31
4 3 The shock boundary layer interaction over a flat plate	31
4 3 1 Grid generation and the boundary conditions	31
4 3 2 Analysis of the shock boundary layer interaction	32
4 3 3 Conclusions	33
4 4 Two-dimensional analyses of flow over a backward facing step	33

4 4 1 Grid generation and the boundary conditions	33
4 4 2 Analyses of flow over the backward facing step	34
4 4 3 Conclusions	36
<b>CHAPTER 5</b>	
<b>CONCLUSIONS</b>	68
5 1 Conclusions	68
5 2 Suggestions for Future Work	68
<b>REFERENCES</b>	
	70

## ABSTRACT

The challenge in prediction of compressible flow phenomena is to resolve as accurately as possible the sudden discontinuities of the flow variables associated with shocks. Over the last three decades, extensive research has been carried out in this direction. Different algorithms have been developed to solve Euler and Navier-Stokes equations for compressible flows. The algorithm developed so far can broadly be classified into two categories. One is of central difference type with explicitly imposed artificial dissipation such as MacCormak and Jemson type algorithms. The other is the upwind type namely Steger and Warming, Van Leer splitting where the discretization is made following the physics of flow and the direction in which the information is propagated. It has been thought that the upwind scheme would perform relatively better as it is based on the physics of the flow. The flux vector type of splitting is one that is simple to implement but leads to an inaccurate solution because of its high dissipation properties. This high dissipation can be eliminated by higher order discretization. The Flux difference splitting has shown improved accuracy such as Roe's Flux Difference Splitting scheme. However, the flux difference schemes are complex to implement and takes more computational time. Recently a scheme named as "Advective Upstream Splitting Method (AUSM)" has been developed combining the advantages of both of the above two schemes. The AUSM algorithm has been found relatively simple for codification and also minimum as accurate as Roe's Flux Difference Splitting. Therefore in the present work an attempt is made to develop a flow solver using the AUSM algorithm in the finite volume formulation. The Navier Stokes equations are integrated in the physical plane so that the truncation error associated with the transformation of variables from the physical to computational plane can be eliminated. To split the fluxes at the cell faces following the algorithm, the variables from the cell center are extrapolated by piecewise finite element reconstruction method. The logic is extended to formulate the higher order discretization. To judge the performance of the flow solver, different test cases such as flow over a bump with subsonic and supersonic conditions, both inviscid and viscous flows, flow over a flat plate with shock boundary layer interactions are computed. The predicted results illustrate the flow solver developed is accurate enough in resolving the boundary layer.

growth, formation of shock associated with compressible flows with an accuracy acceptable for engineering applications

Another objective of the present thesis work is to find the applicability of the flow solver to predict the complex nature of the turbulent flow by Large Eddy Simulation (LES). The huge computational resource required in performing a direct numerical simulation with moderate Reynolds number applications and over complex engineering geometries makes it a distant approach. The practical engineering problem can now be tackled with LES where the Larger eddies are resolved directly and the smaller eddies, which are universal in nature, are modeled by a suitable Subgrid Scale Model. Thus we have incorporated LES in the present solver to resolve the pattern of flow over a backward facing step. This is to judge the suitability of the flow solver in LES calculation. However for the limited computational facility available the analysis is restricted only in two-dimension. It has been seen that the solver is able to predict the vortex structure generated downstream of the step. Further the averaged velocity field has been found to match reasonably well with the experimental data.

## NOMENCLATURE

$x, y$	Cartesian co-ordinates
$u$	velocity component in $x$ -direction
$v$	velocity component in $y$ -direction
$\rho$	density
$c$	speed of sound
$C_p$	specific heat at constant pressure
$C_v$	specific heat at constant volume
$E$	total energy
$p$	pressure
$T$	temperature
$\tau_{ij}$	stress tensor
$h$	heat transfer co-efficient = $q_w/(T_{01}-T_w)$
$M$	Mach number
$Re$	Reynolds Number
$y^+$	law-of-the wall coordinate
$F, G$	flux vectors
$H$	source terms vector
$U$	solution vector
$Pr, Pr_t$	Prandtl Numbers
$q_i$	heat flux vectors
$R$	gas constant
$k$	wave number
$\bar{S}$	surface normal
$ \bar{S} $	local strain rate
$\gamma$	ratio of specific heat = $C_p/C_v$
$\delta$	boundary layer thickness
$\Delta$	small increment
$\delta_{ij}$	Kronecker Delta
$\mu, \mu_t$	molecular and turbulent viscosity

$\xi, \eta$	curvilinear coordinate
$\nu$	kinematic viscosity
$\Omega_{ij}$	cell volume
$\Delta t$	time step
CFL	Courant-Friedrich-Lewis number

## Subscripts

0	stagnation condition
1	inlet plane
2	exit plane
w	wall condition
is	isentropic condition
$i,j$	logical cell indices in space
t	turbulent
$\theta$	momentum thickness
$\infty$	freestream condition

## Superscripts

n	time level
-	space-averaged quantity
$\sim$	density-weighted space-averaged quantity

## LIST OF FIGURES

Fig 3 1 Cell configuration in Finite Volume Method	21
Fig 3 2 Cell configuration for calculation of stresses	22
Fig 4 1 Computational mesh for the channel flow with a 4% thick circular arc bump for the Euler calculation	37
Fig 4 2 Computational mesh for the channel flow with a 4% thick circular-arc bump for the Navier-Stokes solution	38
Fig 4 3 Effect of grid refinement of the surface Mach number distribution for the Navier-Stokes solution	39
Fig 4 4 Mach contours for first order Euler solution of supersonic flow in a channel with a 4% thick circular arc bump, $M_\infty=1.4$	40
Fig 4 5 Mach contours for second order Euler solution of supersonic flow in a channel with a 4% thick circular arc bump, $M_\infty=1.4$	41
Fig 4 6 Mach contours for third order Euler solution of supersonic flow in a channel with a 4% thick circular arc bump, $M_\infty=1.4$	42
Fig 4 7 Comparison of surface Mach number distribution between the first, second and third order accurate results over the circular arc bump	43
Fig 4 8 Comparison of surface Mach number distribution for the circular arc bump from Euler solution with the computed results of Ni [1982]	44
Fig 4 9 Mach contours for Navier-Stokes solution over the 4% thick circular arc bump	45
Fig 4 10 Skin-friction coefficient with $M_\infty=1.4$ over 4% thick circular arc bump	46

Fig 4 11 Mach contours for Euler solution of subsonic flow ( $M_\infty = 0.5$ ) over 4% thick circular arc bump	47
Fig 4 12 Surface Mach number distribution over a circular arc bump from Euler solution with $M_\infty = 0.5$	48
Fig 4 13 Mach contours for Navier-Stokes solution of subsonic flow ( $M_\infty = 0.5$ ) over a 4% thick circular arc bump	49
Fig 4 14 Surface Mach number distribution over a circular arc bump from Navier-Stokes solution with $M_\infty = 0.5$	50
Fig 4 15 Computational mesh over the flat plate for shock-boundary layer interaction problem	51
Fig 4 16 Schematic view of the shock-boundary layer interaction	52
Fig 4 17 Mach contours for shock wave and boundary layer interaction	52
Fig 4 18 Comparison of skin friction coefficient between the experimental and the predicted value for the shock boundary layer interaction problem	53
Fig 4 19 Effect of shock wave on the boundary layer of supersonic flow	54
Fig 4 20 Grid over the backward facing step	55
Fig 4 21 Stream function plots at different instant of time downstream of the backward facing step	56-58
Fig 4 22 Vorticity plots at different instant of time downstream of the backward facing step	59-60

Fig 4 23 Average streamwise and cross-streamwise components of velocity

61-63

Fig 4 24 Average turbulent intensities

63-67

# CHAPTER – 1

## INTRODUCTION

The flow fields in engineering applications are associated with turbulence, mixing, separation and transition. An appropriate flow solver together with an accurate turbulence model is always necessary to predict these kinds of flow and heat transfer phenomena. Even with the sophisticated turbulence model and solution algorithms, it is very difficult to predict properly the sharp changes of flow variables across the shock in compressible flow, the thin shear layer and the flow separation. The conventional turbulence models are good for certain engineering applications, but they are not universal in nature. One way is to use the Direct Numerical Simulation, which is restricted to only low Reynolds number applications and on simple geometries because of its high computational cost. Here lies the importance of the Large Eddy Simulation (LES) where flow properties can be evaluated by solving the filtered Navier-Stokes equations in finer grids and modeling the turbulent stresses by a suitable Subgrid Scale Model. However, an appropriate flow solver is needed for LES calculation. The flow solver should be such that it can resolve the complex flow features due to shock-boundary layer interactions and sudden discontinuities that occur in compressible flows with minimal dissipation level. A well-designed flow solver preferably based on an upwind scheme can atleast minimizes the problem. The widely used certain central difference algorithms with explicitly imposed artificial dissipation (like Lax-Wendroff, MacCormak, Jameson algorithms) may not be suitable for LES. At the same time the dissipation level in some Flux Vector Splitting algorithms may corrupt the solution near the sonic point or within the viscous sublayer. On the other hand, though the Roe's flux difference splitting (1982) is reasonably accurate, it is quite difficult for codification and to extend for a three-dimensional problem. Recently a scheme named as "Advection Upstream Splitting Method (AUSM)" (1993) has been developed which has shown to overcome most of these difficulties. This scheme is relatively easy to implement and needs a lower amount of computation. The AUSM seems to be promising even over the Roe's flux-difference-splitting scheme. Therefore an attempt is made to develop a two-dimensional flow solver in finite volume formulation by using the AUSM algorithm.

dimensional compressible Navier-Stokes flow solver in the finite volume formulation based on the AUSM algorithm. The attractive features of it are that equations are integrated in the physical plate so that any complex geometry can be handled properly, and less truncation error would be resulted. The present work is based on the flow solver developed by Sarkar (2000), where the Navier-Stokes equations are solved in the physical plane based on the four-stage Runge-Kutta algorithm in finite volume formulation. The Jameson algorithm used to split the convective fluxes of the Navier-Stokes Equations has been changed by AUSM algorithm. A piecewise finite element reconstruction procedure has been used to extrapolate the flow variables at the cell faces so that the solver would be at least second-order accurate in space. A local transformation procedure has been used to evaluate the viscous stresses in the Navier-Stokes equations. The local time stepping and residual smoothing have been used to accelerate steady state solution of some of the test cases.

Various test cases have been performed to assess the performance of the flow solver for a wide range of flow conditions. It has been seen that the flow solver is able to resolve the shock wave and the separated flow with reasonable accuracy. The objective of a new flow solver was to study the applicability the solver for LES calculation. Thus the solver is used along with a Subgrid Scale Model to predict the flow over a two-dimensional backward facing step with 8:9 expansion ratio. The analysis is done for a very low free-stream Mach number ( $M_\infty=0.128$ ), for which experimental data was available. As it is found that in the near wall region the Smagorinsky model is highly dissipative in nature, a damping function is used in the subgrid scale stress term to minimize the near wall dissipation. The predicted results have been found to match reasonably well with the experimental data.

The thesis consists of four chapters in addition to the first chapter, Introduction, as mentioned below.

A critical review of the existing literature related to different upwind schemes and LES models is presented and documented in **Chapter 2**. Chapter 3 presents the governing equations and the solution technique in finite volume formulation. The thorough explanation of the Smagorinsky model and its modification to capture near wall

turbulence effect is also given and discussed lucidly in Chapter 4, a systematic analysis of the applicability of the upwind solver is presented. The second part of the chapter deals with the computation of flow over a backward facing step by LES. Conclusions based on the present study and some thoughts on the direction of future research work in this field are provided in Chapter 5.

## CHAPTER - 2

### Literature Review

The objective of the work is to develop a flow solver based on the characteristic information of flow so as to use the solver for LES and DNS type calculations. Thus, in the present chapter a review of the literature for various upwind schemes is presented. Some studies on LES computation and subgrid scale models are also discussed.

#### 2.1 Upwind schemes:

The first upwind scheme was developed by Courant et al (1952) based on the characteristic form of the hyperbolic equations, where the discretization is based on the sign of the eigenvalue. The central difference of the hyperbolic equation is unstable near the sonic transition point. It can be shown that one-sided difference leads to the stability of the hyperbolic equation, when the difference is done based on the characteristic eigenvalue of the equation. The scheme of Godunov (1959) comes from the local exact solution of the Euler equations, which is strictly conservative in nature. Here the solution was considered as piecewise constant over each mesh cell at a fixed time and the evaluation of the flow at the next time step results from the wave interactions at the boundaries between the adjacent cells. The solutions to the Riemann problem at each cell interface produces a perturbation of the fluid state resulting from the propagating waves over the time interval  $\Delta t$ .

The scheme developed by Warming and Beam (1976) is a second-order upwind scheme. The upwinding of the convective fluxes is performed by modification of the corrector term of the MacCormack scheme. One-sided difference is used instead of the central differencing whenever the local characteristic speed was found to be of the same sign. It was found that switching from fully MacCormack to the upwind scheme loses the strict conservation. A spatially transmission operator was derived for switching from the former to the latter to make it fully conservative in nature. This is essential for capturing of the shock waves in the flow domain. However it was found that the scheme has superior dissipative and dispersive properties than those of the central schemes.

Morrietti (1979) developed an explicit first-order upwind algorithm by recasting the Euler equation to the characteristic (Riemann) type variables. This algorithm was known as explicit  $\lambda$  scheme. A two-step MacCormack algorithm was used for the time stepping. The variables were discretised by two point windward difference for negative eigenvalue and three point windward difference for the positive eigenvalue at the predictor level, along with three point windward difference for the negative eigenvalues and two point windward difference for the positive eigenvalues at the corrector level. Though it was found that the scheme was well suited for the transitional flows, it was not found to be conservative in nature. The scheme was found to be complicated for the two- and three-dimensional flows and geometry dependent which was not relevant from the physical point of view.

The work of Osher and Enquist (1980) describes the conservative upwind Riemann solvers, which are monotonic in nature. They found it suitable for transonic flows with small disturbances where the compression and the rarefaction waves are used to approximate the shock waves. The work was further modified by Chakravorty and Osher (1983) to analyze a method for treating computational and physical boundaries based on solving initial boundary value Riemann problem. The one dimensional flow, quasi-one dimensional Laval nozzle flow, conical supersonic flow past an aerofoil and Mach 8 supersonic flow past a circular cylinder were simulated by this algorithm and were presented by them in the same year (1983). The results were found to be quite agreeable with the available data.

A remarkable property of the flux vectors of the inviscid gas-dynamic equations is that they are homogeneous functions of degree one. Using that property Steger and Warming (1980) derived the flux vector splitting algorithm of inviscid gas-dynamic equations by one-sided differencing of the fluxes depending on their characteristic eigenvalues. Both explicit and implicit finite difference algorithms were derived. In the explicit algorithm, MacCormack algorithm was modified in such a way that the forward difference is applied to the predictor step and backward difference in the corrector step and only one-sided differencing was allowed to make it a completely upwind algorithm. Thus the stability bound was increased to 2 for one-dimensional case. Several numerical experiments on one and two-dimensions were performed and found to be agreeable with the actual results. However it was found that the split fluxes are not always continuous and shows

non-differentiability at sonic transition points This happens because of the eigenvalue of the characteristic equation changes its sign leading to the numerical oscillations near the transition or at the sonic points These oscillations can be reduced by introducing a small dissipation parameter in calculating the eigenvalues of the characteristic equations (Burning P G and Steger J L (1982)) The more efficient approach is to split the fluxes in such a way that the slopes of the flux components tends to zero at the transition point, so that no discontinuity would be maintained at the sonic point as suggested by Van Leer (1982) In such cases the fluxes and the associated Jacobians are made continuous functions of the Mach number and expressed as the polynomial of the lowest possible order The scheme was found to be more robust in capturing the strong shock discontinuity as compared to Steger and Warming flux vector splitting scheme

Dadone and Napolitano (1983) modified the explicit lambda model to an implicit one for one-dimensional and two-dimensional flows The compressible conservative equations were expressed in the form of characteristic (Riemann) variables The old time level derivatives were discretised by three-point second order accurate windward difference and unknown derivatives were discretised by two-point first order accurate windward difference Therefore the resultant discretised equations were converted to a block tridiagonal system of equations for one-dimensional flow However to retain the block tridiagonal form for two-dimensional flows they solved the system of equations by ADI scheme The model was further modified to a three-dimensional system of equations for a general orthogonal curvilinear coordinate system However the method appeared computationally expensive

The work of M Ben Arzi et al (1984) describes the solution of generalized Riemann initial value problem with the help of second order accurate Godunov's method They analytically derived the time derivatives both in Lagrangian and Eulerian frame of references even for the flow with the jump discontinuities The scheme is found to be conservative and second order accurate in both time and space.

One of the Godunov types of scheme named as "Flux Difference Splitting" developed by Roe (1981) was an approximate Riemann solver. The fluxes in the Riemann equation were decomposed following the characteristic speed of the wave propagation The upwind dissipation term was calculated by using the local Jacobian matrix of the flux

terms. The variables used to compute this matrix were derived by an average weighted by the square root of the local densities across two sides of a cell face. The scheme was found to be first order accurate in space and strictly conservative in nature. Another good feature of the scheme was that it was able to capture the discontinuity and shock more accurately than flux vector splitting algorithms.

The interesting feature of the Steger and Warming flux-vector splitting is its simplicity in implementation and that of Roe flux-difference splitting is its accuracy. These properties were combined by Liou and Steffen (1993) to get a new type of scheme named as “Advection Upstream Splitting Method (AUSM)”. The convective and the pressure terms were separately discretised in this method. The upwinding of the convective terms was made depending on the cell interface velocity, which was obtained by splitting the Mach number at the cell interface following the Van-Leer splitting. The pressure was weighted by using the polynomial expression of the characteristic speeds ( $M \pm 1$ ). The scheme is relatively easier to implement and also needs lower amount of computation time than FDS scheme. Further the tested results indicated that the scheme could be implemented over any complex geometry with accuracy as high as Roe’s FDS scheme. The dissipation level and the entropy generation within the viscous layer is minimal even compared with the Roe’s scheme and thus it resolved correctly the nose region a supersonic blunt body. It has been felt the scheme would be a suitable for LES/DNS type calculation for complex geometries.

## 2.2 LES computations:

The DNS results appeared so far in the open literature are restricted to simple geometries and for low Reynolds number flows due to high computational time. An alternative is to perform LES calculation where the large scale eddies are captured and the smaller scale eddies which are more universal in nature are modeled. A brief discussion on LES and subgrid scale (SGS) models are presented. The governing equations of turbulent flows are given in LES by filtering the Navier-Stokes equations. The turbulence can be thought of superposition of wakes with different wave numbers. The large-scale motions generated by the larger wakes are flow dependent where the small-scale wakes are found to be universal in nature. To eliminate the subgrid scale fluctuations it is necessary to apply a filtering operation on Navier-Stokes equations that essentially cuts off the wavelength smaller than  $K_c$  (the characteristic wave number defined to be  $\pi/\Delta$ , from the Nyquist

criterion, where  $\Delta$  is the filter width) In that sense, for a large eddy simulation at a practical Reynolds number should have a filter cut off at a wave number in the inertial range SGS models should model the range at which energy decays exponentially

## 2 2 1 Filtering approach

Different filtering operations are required for different levels of turbulence Germano (1986), Moin and Kim (1982), Germano (1992) tested many filter previously The Gaussian filter was found to be most suitable because it has the same expressions as in physical as well as in Fourier space Erlebacher et al (1992) and others made the similar conclusions But for the wall-bounded flows variable length filters should be adopted because of the variation of turbulent length scale perpendicular to the wall as suggested by Moin et al (1982) Several other filters were tested among which top hat filter is widely used because of simplest expression in Fourier space

## 2 2 2 Modelling of SGS terms

A basic ingredient that characterizes the subgrid models used in LES is that their characteristic length-scale is given by the grid size As a consequence simple algebraic models or one-equation turbulence models were adopted The simplest one is Smagorinsky model (1963) The model was adopted by correlating the anisotropic deviatoric part of the stress to the kinematic diffusivity It was found that the Smagorinsky model of eddy viscosity has a one to one correlation with the local strain rate tensor and it is also found to be independent of the filtering operation The particular type of averaging was reflected over  $C_s$  (the Smagorinsky constant) and  $\Delta$  For isotropic turbulence the value of  $C_s$  was analytically determined by Lilly in 1987 From his calculation  $C_s$  was found to be 0.18 But in general to avoid excessive subgrid scale dissipation  $C_s$  is limited to 0.1 This makes the model to behave reasonably well for free-shear flows It was also seen from the work of Deodoroff (1970) and Schumann (1975) that this model is able to predict the characteristics of turbulent channel flow However, it was found that in the near-wall region where the viscous stress is predominant the Smagorinsky model is too much dissipative in nature So the Smagorinsky model failed to detect the viscous sublayer and the buffer layer for a wall bounded flow In such cases the wall model should be adopted and some damping functions should be used to make the eddy-viscosity negligibly small very near the wall The following modification of the Smagorinsky constant can be as,  $C_s=0.1[1.0-\exp\{-(y^+/25)\}^3]^{1/2}$  where  $y^+$  is the non-

dimensional distance away from the wall Bui (1999) suggested the same approach to simulate compressible flow inside a square duct In 1992 Arnal and Friedrich used a different version of this model by replacing  $C_s \Delta$  with  $\min(C_s \Delta, l_m)$ , where  $l_m$  is the mixing length in the near-wall region derived from Nikuradse (1933) The Smagorinsky constant coupled with the damping function was also used by M Breuer and W Rodi (1994) to analyze flow over a 180° bent duct, and B J Boersma et al (1994) for the flow simulation inside an electronic flow-meter Similarly others adopted the same procedure like T G Thomas et al (1994) where  $C_s \Delta$  was replaced by  $\min(C_s \Delta, k l_m \Gamma(l_w^+))$  and  $\Gamma(l_w^+) = 1 - \exp(-l_w^+/A^+)$ , and M Manhart et al (1994) where  $C_s \Delta$  is replaced by  $\min(k x_n \text{ and } C_s \Delta)$  and  $x_n$  was the normal distance for simulation of flow over a cylinder It is also possible to use different values of  $C_s$  at different time as suggested by A Andren et al (1994) Thus,  $C_s$  is to some extent flow dependent

### 2 2 3 Scale-similarity and mixed Models

The eddy viscosity closure assumed a one to one correlation between the subgrid scale and the large-scale strain tensor However in actual cases the correlation between these two quantities was found to be very less This lack of correlation made Bardina et al (1980) to propose an alternative subgrid scale model called scale-similarity model This model is based on the double filtering of the flow variables The basic idea originates from the interaction between the smallest scale eddy of the resolved scale and the largest scale eddy in the subgrid scale that causes the energy back scatter from the subgrid scale to the resolved scale The inclusion of the Leonard and Cross-term in the subgrid scale tensor made the model capable in the prediction of subgrid scale backscatter of the kinetic energy Indeed the good correlation with the DNS data made the model highly important, which was further modified to the dynamic model

### 2 2 4 Dynamic SGS modelling

The basic idea of the dynamic SGS model, developed by Germano et al (1991) was to improve the Smagorinsky model by setting  $C_s$  different values for different mesh nodes at each time step, which attempts to self-adjust the dissipation by subgrid scale stresses This model was developed basically by double filtering of the Navier-Stokes equations At first a grid level filter was used to resolve the fluctuating velocity field Next a test level filter that was generally larger in magnitude was applied on the filtered velocity

field The excess of fluctuating resolved velocity field and filtered resolved velocity field obtained from test filter gives the information of the value of the constant

$$C_{\text{dyn}}(x, y, z) = \frac{L_{kl}S_{kl}}{2M_{kl}S_{kl}}, \text{ where } L_{kl} \text{ is the Leonard term denoted as}$$

$$L_{kl} = \widehat{\overline{u}}_k \widehat{\overline{u}}_l - \widehat{\overline{u}_k \overline{u}_l},$$

$$M_{kl} = \widehat{\Delta^2} |\widehat{\overline{S}}| \widehat{|S_{kl}|} - \widehat{\Delta^2} |\widehat{\overline{S}}| \widehat{|S_{kl}|}, \text{ where } S_{kl} \text{ is the local strain rate and } |\widehat{\overline{S}}| = (2 \widehat{\overline{S}_{kl}} \widehat{\overline{S}_{kl}})^{1/2}$$

However the model was proved to be mathematically inconsistent by Ghosal et al (1995), because C was taken to be independent of the test filter width From the test using channel flow data from direct numerical simulations, Germano et al (1991) shown that the denominator of the expression could locally vanish or become sufficiently small, thereby leading to computational instability. Later Lilly (1992) adopted a least square procedure to minimize the error so that the expression of C can be given as

$$C = \frac{L_{kl}M_{kl}}{2M_{kl}M_{kl}}$$

Sometimes this dynamic constant causes the instability of the simulation as it varies in a wide range over the whole flow domain producing a strong gradient of  $v_t$ . It is also possible that at a particular grid point the constant remains negative for a larger period of time It leads to subgrid scale energy transfer to the resolved scale causing the excessive backscatter of energy To avoid this some temporal and spatial averaging may be done along the homogeneous direction The simplest way to modify the constant suggested by P. Sagaut et al (1994) is to truncate the dynamic constant by the following constraints

$$1 \quad \frac{1}{Re} + v_t \geq 0$$

$$2 \quad C_{\text{dyn}} \leq C_{\text{max}}$$

The maximum value of the dynamic constant is taken as the square of Smagorinsky constant This model can be able to predict the near wall boundary layer situations In another way to restrict the value of C to a time independent function and to allow variations with low frequencies, a low pass filtering method was chosen (M Breuer and W Rodi (1994)) C can be given as

$$C_{\text{filtered}}^{n+1} = (1 - \varepsilon) C^n + \varepsilon C^{n+1},$$

With value of  $\varepsilon \sim 10^{-3}$  All frequencies of oscillation damps out with low frequencies of oscillation remains Akselvoll and Moin (1993) also adopted the method for backward facing step, which has still one homogeneous direction

The mathematical inconsistency presented in Germano's model was removed by the newly developed constrained dynamic localization model as proposed by Ghosal et al (1995), which can be imposed on flow without any homogeneous direction. The constant  $C \geq 0$  was in this model in order to derive an integral equation for  $C$ . However, this model shows no backscatter, which is essential for simulation of transitional flows. Another model was proposed by the same author (known as k-equation localization model) can be able to transfer subgrid scale energy to the resolved scale by the inclusion of the transport equation for subgrid scale kinetic energy. However these two models are still not widely used for inclusion of two more integral equations and one transport equation.

## 2.2.5 SGS for compressible flows

Yoshizawa (1986) suggested the first compressible SGS model for weakly compressible shear flow with the aid of multi-scale direct interaction approximation. The model had included Leonard and cross terms that are generally neglected in the Smagorinsky model. In fact the effect of back scatter due to cross-term is not clear for the Smagorinsky model. This is only applicable for the cross term because of the use of an asymptotic expansion about an incompressible state. The model was further modified to the compressible flow calculation by Erhebacher et al (1992), Vreman et al (1994), Squires et al (1991) and Moin et al (1991). The model presented by Erhebacher et al contains the crossed and Leonard terms both for modelling of the subgrid scale part of the momentum and energy equations, which was otherwise neglected by Yoshizawa's model. Though the isotropic part of the turbulent stress tensor was modeled it was found that the model correlates poorly with the DNS of isotropic turbulence presented by Speziale et al (1988). Bui (1999) confirmed the same result with inclusion of this term in the LES model. However, with the low turbulent Mach number, which is generally encountered in the practical cases, the isotropic part of the turbulence is an order of magnitude lower than the thermodynamic pressure. So, it is generally neglected in the turbulent flow simulation of low Mach number flows. This was also supported by Squires et al. (1991) and Vreman et al (1994). This model was further improved Moin et al (1991), Squires et al (1991), where the Smagorinsky constant was determined dynamically in space and time so that

the model can be made flow independent However the models are restricted only within the low Mach number range and simulation of high Reynolds number and high Mach number flows are still not found in open literature

### **2.3 Conclusions:**

The present review of literature reveals that a significant progress has been made in the development of upwind schemes and different types of LES models Applications of these models on relatively simple geometries illustrate that the models are successful to predict the largest structure of turbulence with high accuracy However the simulation of high Reynolds number flow over the complicated geometries is still a formidable task and there is further scope of improvement in this area

## CHAPTER – 3

# GOVERNING EQUATIONS AND NUMERICAL PROCEDURE

### 3.1 Introduction

The main objective of the present work is to develop a two-dimensional Navier-Stokes solver by using the AUSM algorithm. Also the present study explores the ability of the Smagorinsky LES model to simulate the flow over a backward facing step. Thus, in this chapter, both the Euler and the Navier Stokes equations, the LES model and the numerical technique in discretisation of the governing equations are presented.

### 3.2 Governing equations and LES model

In this chapter, the Euler equations and the Navier-Stokes equations for the laminar and turbulent flows are presented. All these equations are presented in the conservative forms and solved in physical plane based on finite volume algorithm. For the turbulent flow, the governing equations can be obtained by filtering (local volume averaging) the Navier-Stokes equations. Further to reduce the equation to a simpler form a density weighted averaging (Favre filtering) has been done. The density weighted averaging leads to a simpler form of the governing equations with terms that are more amenable to physical interpretation. The Subgrid Scale Stresses are modeled by the Smagorinsky model. It should be noted that density-weighted space averaging is used for velocity components and temperature, whereas the space averaging is used for pressure and density.

#### 3.2.1 Flow equations

The time-dependent, two-dimensional, compressible Navier-Stokes equations for laminar flows can be expressed in the conservative form as,

$$\frac{\partial \mathbf{U}}{\partial t} + \frac{\partial \mathbf{F}}{\partial x} + \frac{\partial \mathbf{G}}{\partial y} = \mathbf{H} \quad (3.1)$$

where,

$$\mathbf{U} = \begin{pmatrix} \rho \\ \rho u \\ \rho v \\ E \end{pmatrix}, \quad \mathbf{F} = \begin{pmatrix} \rho u \\ \rho u^2 + p - \tau_{xx} \\ \rho uv - \tau_{xy} \\ (E + p - \tau_{xx})u - \tau_{xy}v + q_x \end{pmatrix}$$

$$G = \begin{pmatrix} \rho v \\ \rho u v - \tau_{yx} \\ \rho v^2 + p - \tau_{yy} \\ (\bar{E} + p - \tau_{yy})v - \tau_{yx}u + q_y \end{pmatrix} \quad \text{and} \quad H = \begin{pmatrix} 0 \\ 0 \\ 0 \\ 0 \end{pmatrix} \quad (3.2)$$

are state vector, convective flux vectors in x and y directions and source terms vector respectively. The stress tensor and the heat flux vector are given in Cartesian coordinates as,

$$\tau_{ij} = \mu \left[ \left( \frac{\partial u_i}{\partial x_j} + \frac{\partial u_j}{\partial x_i} \right) - \frac{2}{3} \delta_{ij} \frac{\partial u_k}{\partial x_k} \right] \quad \text{and} \quad \bar{q}_i = - \frac{\mu C_p}{Pr} \frac{\partial T}{\partial x_i} \quad (3.3)$$

In the present study, the laminar viscosity coefficient  $\mu$  is assumed to be a function of temperature only, and is evaluated following the Sutherland's law which is given by,

$\mu = C_1 \frac{(T)^{3/2}}{T + C_2}$ , where  $C_1$  and  $C_2$  are constants for a given gas. For air at moderate temperatures,  $C_1 = 1.458 \times 10^{-6}$  kg/(ms  $^{\circ}$ K) and  $C_2 = 110.4^{\circ}$ K. The perfect gas equation of state  $p = \rho RT$ , is considered to be applicable.

For an inviscid flow, Eq 3.1 remains the same where the elements of the column vectors are simplified. Thus, omitting the viscous terms from the Navier-Stokes equations, the Euler equations in the conservative form are,

$$\frac{\partial U}{\partial t} + \frac{\partial F}{\partial x} + \frac{\partial G}{\partial y} = 0 \quad (3.4)$$

where,

$$U = \begin{pmatrix} \rho \\ \rho u \\ \rho v \\ E \end{pmatrix} \quad F = \begin{pmatrix} \rho u \\ \rho u^2 + p \\ \rho uv \\ (\bar{E} + p)u \end{pmatrix} \quad \text{and} \quad G = \begin{pmatrix} \rho v \\ \rho uv \\ \rho v^2 + p \\ (\bar{E} + p)v \end{pmatrix} \quad (3.5)$$

### 3.2.2 Governing equations for LES

The governing equations for compressible turbulent flows can be obtained by filtering the Navier-Stokes equations. The equations are similar to that of the laminar flow equations,

but there is additional subgrid scale stress terms in momentum and energy equations

They can be written as

$$\frac{\partial U}{\partial t} + \frac{\partial F}{\partial x} + \frac{\partial G}{\partial y} = 0$$

$$U = \begin{pmatrix} \bar{\rho} \\ \bar{\rho}\tilde{u} \\ \bar{\rho}\tilde{v} \\ \tilde{E} \end{pmatrix}, \quad F = \begin{pmatrix} \bar{\rho}\tilde{u} \\ \bar{\rho}\tilde{u}^2 + \bar{p} - \bar{\tau}_{xx} \\ \bar{\rho}\tilde{u}\tilde{v} - \bar{\tau}_{xy} \\ (\tilde{E} + \bar{p} - \bar{\tau}_{xx})\tilde{u} - \bar{\tau}_{xy}\tilde{v} + \bar{q}_x \end{pmatrix} \text{ and}$$

$$G = \begin{pmatrix} \bar{\rho}\tilde{v} \\ \bar{\rho}\tilde{u}\tilde{v} - \bar{\tau}_{yx} \\ \bar{\rho}\tilde{v}^2 + \bar{p} - \bar{\tau}_{yy} \\ (\tilde{E} + \bar{p} - \bar{\tau}_{yy})\tilde{v} - \bar{\tau}_{yx}\tilde{u} + \bar{q}_y \end{pmatrix} \quad (3.6)$$

The stress tensor and the heat flux vector can be reduced to,

$$\bar{\tau}_{ij} = \mu \left[ \left( \frac{\partial \tilde{u}_i}{\partial x_j} + \frac{\partial \tilde{u}_j}{\partial x_i} \right) - \frac{2}{3} \delta_{ij} \frac{\partial \tilde{u}_k}{\partial x_k} \right] + \tau_{tij} \quad \text{and} \quad \bar{q}_i = - \frac{\mu C_p}{Pr} \frac{\partial \tilde{T}}{\partial x_i} + \bar{q}_ti \quad (3.7)$$

The bar in the equations (3.6) and (3.7) denotes a flow quantity, defined as

$\bar{f} = \int_D G(\bar{x} - \bar{x}') f(\bar{x}') d\bar{x}'$ , where  $G$  is a special filter and the integral is over the flow domain  $D$

domain  $D$  The tilde quantities in the flow equations can be obtained by Favre-filtering

$$\text{given as } \tilde{f} = \frac{\overline{\rho f}}{\overline{\rho}}$$

The turbulent stress quantities  $\bar{\tau}_{tij}$  and  $\bar{q}_{ti}$  have been modeled by a Subgrid Scale Model (SGS) model as used by Bui (1999). It has been discussed in detail in the next section

### 3.2.3 Subgrid Scale Model

The subgrid stress term in the momentum equation is  $\bar{\tau}_{tij}$

where,

$$\bar{\tau}_{tij} = (\tilde{u}_i \tilde{u}_j - \tilde{u}_i \tilde{u}_j) \bar{f}$$

This term can be modeled by

$$\bar{\tau}_{tij} = 2C\bar{\rho}\Delta^2 |S| (\tilde{S}_{ij} - \frac{1}{3}\tilde{S}_{mm}\delta_{ij}) - \frac{1}{3}q^2\delta_{ij} \quad (3.9)$$

where,

$$q^2 = \bar{\tau}_{t_{11}}$$

is the trace of the SGS Reynolds stress tensor. The filtered velocity gradient tensor is

$$\tilde{S}_{ij} = \frac{1}{2} \left( \frac{\partial \tilde{u}_i}{\partial x_j} + \frac{\partial \tilde{u}_j}{\partial x_i} \right)$$

and

$$|\tilde{S}| = (2 \tilde{S}_{ij} \tilde{S}_{ij})^{1/2}$$

In Eq. 3.9, C is a constant to be determined according to the particular SGS model used. For Smagorinsky SGS model, a value of  $C=0.1$  is chosen which is the square of the Smagorinsky constant  $C_s$ .

For the wall bounded turbulent flow, the Smagorinsky model was found to be too much dissipative near the wall. So this Smagorinsky model has to be modified near the wall to capture the viscous sublayer there. A typical way is to vary the Smagorinsky constant dynamically throughout the flow domain. But this process was found to be too much computationally inefficient even for simpler flows. A simpler way is to multiply the Smagorinsky constant with the Van-Direst damping function to make the eddy viscosity negligibly small near the wall. The resultant constant is

$$C=0.1(1.0 - \exp\left(-\left(\frac{y^+}{25}\right)^3\right)) \quad (3.10)$$

Where  $d^+$  is the normal distance from the wall in wall units, defined as

$$y^+ = \frac{\rho u_\tau d}{\mu}$$

and the friction velocity is defined as

$$u_\tau = \sqrt{\frac{\tau_w}{\rho}}$$

After the step the normal distance is calculated from two wall directions and is reduced to be

$$d = \frac{2xy}{x + y + \sqrt{x^2 + y^2}} \quad (3.11)$$

The filter width  $\Delta$  is chosen to be the grid spacing size, which is defined as  $\sqrt{A}$ , where A is the area of the cell.

From a priori test done by Vreman et al it was found that the inclusion of the SGS isotropic stress tensor leads to instability of the system of equations So in our study we have neglected the isotropic part of the turbulence With the term  $q^2$  omitted, the SGS stresses included in the momentum equations by simply replacing the laminar viscosity coefficient  $\mu_{eff} = \mu + \mu_{SGS}$  where,  $\mu_{SGS} = C_p \bar{\rho} \Delta^2 |\bar{S}|$ , and in the energy equation it is

$$\text{included as } q_{eff} = q + q_{SGS}, \text{ where } q_{SGS} = -\frac{\mu_{SGS} C_p}{Pr_t} \frac{\partial \tilde{T}}{\partial x_1}$$

### 3.3 Numerical scheme

The unsteady, two-dimensional Euler and Navier-Stokes equations are solved in the infinite volume by using the four-stage Runge-Kutta time-stepping scheme, in conjunction with different accelerating techniques

The computational domain is divided into quadrilateral finite volume cells, Fig 3 1 For each cell, the unsteady two-dimensional Navier-Stokes equations Eqs 3.1 can be represented in the integral form as,

$$\frac{\partial}{\partial t} \int_{\Omega} U d\Omega + \int_S \bar{Q} d\bar{S} = 0 \quad (3.12)$$

where,  $\Omega$  denotes the volume of the control volume being considered,  $d\bar{S}$  is the surface normal,  $\bar{Q} = (F, G)$  is the flux vector and  $U$  is the state vector

A simple discretised form of the Eq 3.12, for a discrete cell  $(i, j)$  Fig. 3 1, is given by,

$$\frac{d}{dt} (\Omega_{i,j} U_{i,j}) + \oint_S (F dy - G dx) = 0 \quad (3.12a)$$

$$\frac{d}{dt} (\Omega_{i,j} U_{i,j}) + \bar{Q}(U)_{i,j} = 0 \quad (3.12b)$$

where,  $\Omega_{ij}$  is the volume of the discrete cell and  $\bar{Q}(U)_{ij}$  are finite volume approximations for the net convective and diffusive fluxes out the discrete cell The indexing scheme and the integration direction of the line integral is shown in the Fig 3 1 As an example for the east face of the cell the values of  $\Delta x_1$  and  $\Delta y_1$  are given as

$$\Delta x_1 = x_{i+1,j+1} - x_{i+1,j}$$

$$\Delta y_i = y_{i+1,j+1} - y_{i+1,j}$$

and  $F_k$  and  $G_k$  are x and y direction flux averages on the  $k_{th}$  cell face given as,

$$F_k = [\rho u, \rho uu + p, \rho vu, (E+p)u]^T$$

$$G_k = [\rho v, \rho vu, \rho vv + p, (E+p)v]^T$$

The integral  $\bar{Q} d\bar{S}$  in Eq 3.12 is thus taken care of by the combination of the convective and diffusive fluxes out of the discrete cell. For a cell-centered scheme,  $U_{i,j}$  is assumed to be at the center of the cell. The convective term is computed by modifying the "Advection Upstream Splitting Method", developed by Liou and Steffen (1993) for the arbitrary finite volume cells and making it up to the second order accurate by the method developed by Coirier (1994). For the diffusive flux, the calculation procedure of the viscous derivatives is discussed in a later section.

### 3.3.1 Calculations of the convective fluxes

For the calculation of the advective fluxes the solution procedures are reconstruction and flux computation. The principal aim of the reconstruction procedure is to make higher order upwinding of the convective terms. For this reconstruction procedure the primitive variables ( $\rho, u, v, p$ ) are calculated at the cell center and extrapolated at the cell faces to discretize the convective terms. For the second order upwinding each of the four primitive variables  $\rho, u, v, p$  are assumed to vary linearly within the finite volume as

$$\phi_x = \bar{\phi} + U_x(x - \bar{x}) + U_y(y - \bar{y}) \quad (3.13a)$$

where,  $\phi$  will be any of the above four variables. For the third order upwinding process these variables are calculated as

$$\phi_x = \bar{\phi} + U_x(x - \bar{x}) + U_y(y - \bar{y}) + U_{xx}(x - \bar{x})^2/2 + U_{yy}(y - \bar{y})^2/2 + U_{xy}(x - \bar{x})(y - \bar{y}) \quad (3.13b)$$

Following these extrapolation formulae the values of the variables can be extrapolated to the cell faces. The bars in equation (3.13a and 3.13b) denote the cell averaged value and  $U_x, U_y, U_{xx}, U_{yy}$  and  $U_{xy}$  denote the gradients within the cells.

The gradients  $U_x, U_y$  are computed by the method used by Coirier (1994). The value of  $U_x, U_y$  in the target cell is computed by the least square procedure that minimizes the sum of the square of the differences between the values of reconstruction polynomial of the

neighbouring cells and that of the target cell. For a two dimensional control volume the minimization procedure can be written as

$$\begin{bmatrix} a_1 & b_1 \\ b_1 & a_2 \end{bmatrix} \begin{bmatrix} U_x \\ U_y \end{bmatrix} = \begin{bmatrix} c_1 \\ c_2 \end{bmatrix}$$

$$a_1 = \sum_{i=1}^4 (\bar{x}_i - \bar{x}_0)^2$$

$$a_2 = \sum_{i=1}^4 (\bar{y}_i - \bar{y}_0)^2$$

$$b_1 = \sum_{i=1}^4 (\bar{x}_i - \bar{x}_0)(\bar{y}_i - \bar{y}_0)$$

$$c_1 = \sum_{i=1}^4 (\bar{U}_i - \bar{U}_0)(\bar{x}_i - \bar{x}_0)$$

$$c_2 = \sum_{i=1}^4 (\bar{U}_i - \bar{U}_0)(\bar{y}_i - \bar{y}_0)$$

where,  $i=1-4$  denotes the neighbouring cells and  $i=0$  denotes the target cell. These gradients are used to extrapolate the values of the dependent variables on the cell faces. The values of  $U_{xx}$ ,  $U_{yy}$  and  $U_{xy}$  can be calculated by using the same matrix, where

$$a_1 = \sum_{i=1}^4 (\bar{x}_i - \bar{x}_0)^2$$

$$a_2 = \sum_{i=1}^4 (\bar{y}_i - \bar{y}_0)^2$$

$$b_1 = \sum_{i=1}^4 (\bar{x}_i - \bar{x}_0)(\bar{y}_i - \bar{y}_0)$$

$$c_1 = \sum_{i=1}^4 (\bar{U}_{x_i} - \bar{U}_{x_0})(\bar{x}_i - \bar{x}_0)$$

$$c_2 = \sum_{i=1}^4 (\bar{U}_{y_i} - \bar{U}_{y_0})(\bar{x}_i - \bar{y}_0)$$

Following these expressions any dependent variable at the east, west, north and south faces of any cell for second order upwinding method can be written as

$$\phi_{Eij} = \phi_{ij} + U_{xij} (x_E - \bar{x}_{ij}) + U_{yij} (y_E - \bar{y}_{ij})$$

$$\phi_{Nij} = \phi_{ij} + U_{xij} (x_N - \bar{x}_{ij}) + U_{yij} (y_N - \bar{y}_{ij})$$

$$\phi_{Wij} = \phi_{ij} + U_{xij} (x_W - \bar{x}_{ij}) + U_{yij} (y_W - \bar{y}_{ij})$$

$$\phi_{Sij} = \phi_{ij} + U_{xij} (x_S - \bar{x}_{ij}) + U_{yij} (y_S - \bar{y}_{ij})$$

where,

$$x_E = (x_{i+1,j} + x_{i+1,j+1})/2$$

$$x_N = (x_{i+1,j+1} + x_{i,j+1})/2$$

$$x_W = (x_{ij} + x_{i,j+1})/2$$

$$x_S = (x_{ij} + x_{i+1,j})/2$$

The next step is to calculate the inviscid fluxes at the cell faces throughout the control volume. The inviscid flux is approximated by the AUSM scheme as presented by Liou and Steffen (1993). For this scheme the normal Mach number at each face is calculated from the normal velocity vectors. In each face of the cell this normal Mach number is used to calculate the normal flux. For this the inviscid normal flux is divided into the convective and the pressure components given as

$$F = [\rho u, \rho uu, \rho vu, (E+p)u]^T + [0, p, 0, 0]^T = F^{(c)} + [0, p, 0, 0]^T$$

$$G = [\rho u, \rho vu, \rho vv, (E+p)v]^T + [0, 0, p, 0]^T = G^{(c)} + [0, 0, p, 0]^T$$

The effective way of writing the convective flux at any face of the cell is given as

$$F_{1/2}^{(c)} = M_{1/2}^n [\rho a, \rho ua, \rho va, (E+p)a]^T_{LR}$$

$$G_{1/2}^{(c)} = M_{1/2}^n [\rho a, \rho ua, \rho va, (E+p)a]^T_{LR}$$

where,

$$(•)_{LR} = (•)_L \text{ if } M_{1/2}^n \geq 0,$$

$$= (•)_R, \text{ otherwise}$$

The advective Mach number  $M_{1/2}^n$  is computed from the split Mach numbers  $M_L^n$  and  $M_R^n$ . These split Mach numbers are derived according to the Van-Leer splitting as

$$M^\pm = \pm 1/4(M^n \pm 1)^2, \text{ if } |M^n| \leq 1$$

$$= 1/2(M^n \pm |M^n|), \text{ otherwise}$$

The first order pressure splitting can be expressed as,

$$p^\pm = p(1 \pm M^n)/2, \quad \text{if } |M^n| \leq 1,$$

$$= p(M^n \pm |M^n|)/2M^n, \quad \text{otherwise}$$

Following these the flux formula at any cell face can be expressed as,

$$\begin{aligned}
 F_{1/2} &= \begin{pmatrix} \rho u \\ \rho uu + p \\ \rho vu \\ (E+p)u \end{pmatrix}_{1/2} = \frac{1}{2} M_{1/2}^n \left[ \begin{pmatrix} \rho a \\ \rho ua \\ \rho va \\ (E+p)a \end{pmatrix}_L + \begin{pmatrix} \rho a \\ \rho ua \\ \rho va \\ (E+p)a \end{pmatrix}_R \right] - \frac{1}{2} |M_{1/2}^n| \Delta_{1/2} \begin{pmatrix} \rho a \\ \rho ua \\ \rho va \\ (E+p)a \end{pmatrix} \\
 &\quad + \begin{pmatrix} 0 \\ (p_L^+ + p_R^-) \\ 0 \\ 0 \end{pmatrix} \\
 G_{1/2} &= \begin{pmatrix} \rho v \\ \rho vu \\ \rho vv + p \\ (E+p)v \end{pmatrix}_{1/2} = \frac{1}{2} M_{1/2}^n \left[ \begin{pmatrix} \rho a \\ \rho ua \\ \rho va \\ (E+p)a \end{pmatrix}_L + \begin{pmatrix} \rho a \\ \rho ua \\ \rho va \\ (E+p)a \end{pmatrix}_R \right] - \frac{1}{2} |M_{1/2}^n| \Delta_{1/2} \begin{pmatrix} \rho a \\ \rho ua \\ \rho va \\ (E+p)a \end{pmatrix} \\
 &\quad + \begin{pmatrix} 0 \\ 0 \\ (p_L^+ + p_R^-) \\ 0 \end{pmatrix} \tag{3.14}
 \end{aligned}$$

where,  $\Delta_{1/2} \{ \} = \{ \}_R - \{ \}_L$ . Here  $\{ \}_R$  denotes the right side cell of the face considered and  $\{ \}_L$  denotes the left side cell of that face

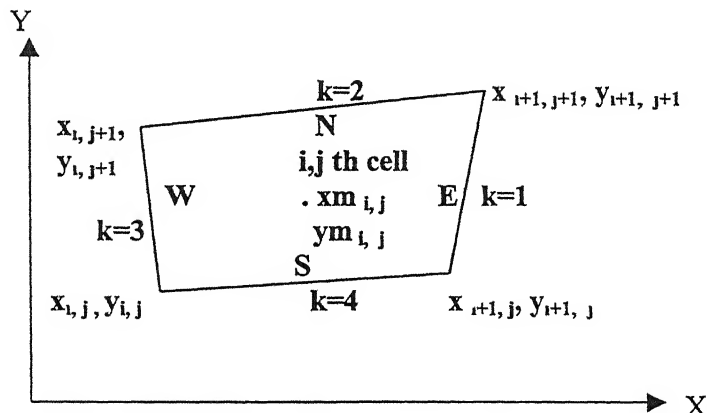


Fig 3.1 Cell configuration in Finite Volume Method

To reduce the time of the computation, on the west and south faces of the cell  $(i,j)$  the respective fluxes are copied from the fluxes of east and north face of the  $(i-1,j)$  th and  $(i,j-1)$  th cells respectively

To limit the values of the gradients of the dependent variables at the boundary cells of the flow domain the effect of the fourth cells ( $(i=4$ , in Fig 3 2) for the lower boundary and  $(i=2$ , in Fig 3 2) for the upper boundary) have not been taken in account For the inviscid flow the boundary condition is imposed by making the normal component of velocity zero on the free surfaces There is only pressure term that remains on those boundaries For the viscous flow simulations making the velocity vector zero at the solid walls imposes the boundary condition At the inlet all the dependent variables are imposed for the supersonic flow and only the pressure term is extrapolated from the first inlet cell for the subsonic flow keeping all the other flow variables imposed at the inlet Similarly at the outlet of the flow domain all the variables are extrapolated for the supersonic flow and only one of the dependent variables is explicitly imposed keeping all other variables extrapolated from the external boundary cell for the subsonic flow

### 3 3 2 Calculation of Viscous Derivatives

The viscous derivatives for the non-orthogonal mesh is evaluated following the Deiwart (1975), by transforming the variables on local co-ordinate system concurrent to the mesh orientation, Fig 3 2

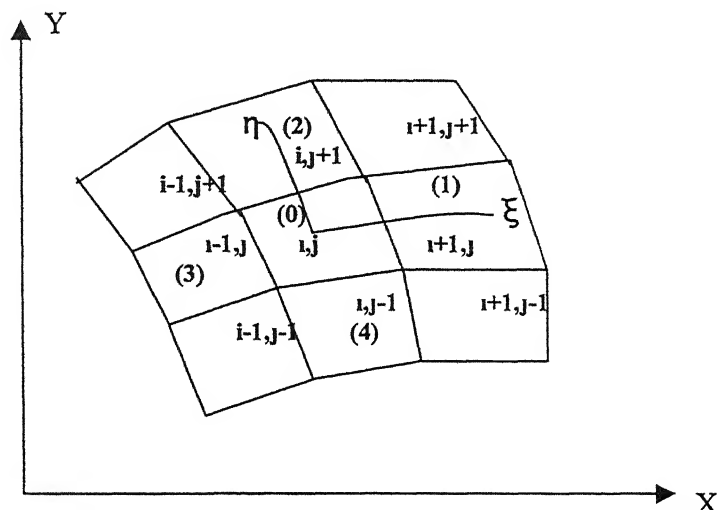


Fig 3 2 Cell configuration for calculation of stresses

The transformation is given by,

$$\begin{aligned}\frac{\partial \phi}{\partial x} &= \frac{\partial \phi}{\partial \xi} \frac{\partial \xi}{\partial x} + \frac{\partial \phi}{\partial \eta} \frac{\partial \eta}{\partial x} \\ \frac{\partial \phi}{\partial y} &= \frac{\partial \phi}{\partial \xi} \frac{\partial \xi}{\partial y} + \frac{\partial \phi}{\partial \eta} \frac{\partial \eta}{\partial y}\end{aligned}\quad (3.15)$$

Here,  $\phi$  is a dummy-dependent variable and  $(\xi, \eta)$  are the local coordinates of the non-orthogonal mesh. The above transformation in matrix form becomes,

$$\begin{bmatrix} \phi_x \\ \phi_y \end{bmatrix} = \begin{bmatrix} \xi_x \eta_x \\ \xi_y \eta_y \end{bmatrix} \begin{bmatrix} \phi_\xi \\ \phi_\eta \end{bmatrix} \quad (3.16)$$

where,  $\phi_x = \frac{\partial \phi}{\partial x}$  and  $\xi_x = \frac{\partial \xi}{\partial x}$  respectively. The other symbols have their usual meanings.

$$\text{Now, } \begin{bmatrix} \xi_x \eta_x \\ \xi_y \eta_y \end{bmatrix} = \begin{bmatrix} x_\xi y_\xi \\ x_\eta y_\eta \end{bmatrix}^{-1} = \frac{1}{J} \begin{bmatrix} y_\eta - y_\xi \\ x_\eta - x_\xi \end{bmatrix}$$

$$\text{where, } J = \begin{vmatrix} x_\xi & y_\xi \\ x_\eta & y_\eta \end{vmatrix} = (x_\xi y_\eta - x_\eta y_\xi) \quad (3.17)$$

$$\text{Hence we have, } \begin{bmatrix} \phi_x \\ \phi_y \end{bmatrix} = \frac{1}{J} \begin{bmatrix} y_\eta - y_\xi \\ x_\eta - x_\xi \end{bmatrix} \begin{bmatrix} \phi_\xi \\ \phi_\eta \end{bmatrix}$$

Therefore,

$$\begin{aligned}\frac{\partial \phi}{\partial x} &= \frac{\Delta \phi_\xi \Delta y_\eta - \Delta \phi_\eta \Delta y_\xi}{\Delta x_\xi \Delta y_\eta - \Delta x_\eta \Delta y_\xi} \\ \frac{\partial \phi}{\partial y} &= -\frac{(\Delta \phi_\xi \Delta x_\eta - \Delta \phi_\eta \Delta x_\xi)}{(\Delta x_\xi \Delta y_\eta - \Delta x_\eta \Delta y_\xi)}\end{aligned}\quad (3.18)$$

For east face

$$\Delta \phi_\xi = \phi_{i+1,j} - \phi_{i,j}$$

$$\Delta \phi_\eta = (\phi_{i+1,j+1} + \phi_{i,j+1} - \phi_{i+1,j-1} - \phi_{i,j-1})/4$$

$$\Delta\theta_\xi = \theta_{m_{i+1,j}} - \theta_{m_{i,j}}$$

$$\Delta\theta_\eta = (\theta_{m_{i+1,j+1}} + \theta_{m_{i,j+1}} - \theta_{m_{i,j-1}} - \theta_{m_{i+1,j-1}})/4$$

For north face,

$$\Delta\phi_\xi = (\phi_{i+1,j} + \phi_{i+1,j+1} - \phi_{i-1,j} - \phi_{i-1,j+1})/4$$

$$\Delta\phi_\eta = \phi_{i,j+1} - \phi_{i,j}$$

$$\Delta\theta m_\xi = (\theta m_{i+1,j} + \theta m_{i+1,j+1} - \theta m_{i-1,j} - \theta m_{i-1,j+1})/4$$

$$\Delta\theta_\eta = \theta m_{i,j+1} - \theta m_{i,j}$$

In the preceding expressions,  $\phi$  denotes the velocity components  $u$  and  $v$  respectively, which are cell-centered variables.  $\theta m$  denotes the center co-ordinates of the finite volume cell

$$\Phi=(u, v), \quad \theta m=(x_m, y_m)$$

If  $\theta_{i,j}$  denotes the co-ordinate of one corner point of the hexahedral finite volume cell, in Fig 3.2, then

$$\theta_{m_{i,j}} = (\theta_{i,j} + \theta_{i+1,j} + \theta_{i+1,j+1} + \theta_{i,j+1})/4$$

where,  $\theta = (x, y)$

This treatment of viscous derivative usually results in central differences and maintains second-order accuracy

### 3.3.3 Time integration

Using a four-stage Runge-Kutta scheme, the system of differential equations, Eqs 3.12b, are advanced in time. It can be written for the  $n$ th time level as,

$$U^0 = U^n$$

$$U^1 = U^0 - \alpha_1 \Delta t R(U^0)$$

$$U^2 = U^0 - \alpha_2 \Delta t R(U^1)$$

$$U^3 = U^0 - \alpha_3 \Delta t R(U^2)$$

$$U^4 = U^0 - \alpha_4 \Delta t R(U^3)$$

$$U^{n+1} = U^4$$

where, at the  $(m+1)$ st stage,

$$R(U^{m+1}) = \frac{1}{\Omega} Q(U^m) \quad (3.19)$$

with  $\alpha_1 = 1/4$ ,  $\alpha_2 = 1/3$ ,  $\alpha_3 = 1/2$ ,  $\alpha_4 = 1/0$

Based on the Fourier stability analysis of a one-dimensional model problem, the four-stage Runge-Kutta time stepping proposed by Jameson et al (1981) appears to be very attractive and is employed for the present work. The CFL number restriction, based on the stability analysis of the model one-dimensional problem, is  $2\sqrt{2}$ , which is relatively higher than most of the explicit schemes.

### 3.3.4 Acceleration Techniques

#### Local Time Stepping

For faster steady state calculation, the locally varying maximum allowable time step is used. The actual time step limit in the present work is expressed as

$$\Delta t = \text{CFL} \left( \frac{\Delta t_c \Delta t_d}{\Delta t_c + \Delta t_d} \right), \text{ where } \Delta t_c \text{ is the limit due to the convective terms, } \Delta t_d \text{ is the limit}$$

due to diffusive terms, and CFL is the Courant-Friedrichs-Lowy number. In particular,

$$\begin{aligned} \Delta t_c &= \frac{\Omega}{\lambda_\xi + \lambda_\eta} \\ \Delta t_d &= \frac{\Omega^2}{K_t (\gamma \mu / \rho \text{Pr}) \left[ |\bar{S}_\xi|^2 + |\bar{S}_\eta|^2 \right]} \end{aligned} \quad (3.20)$$

where,  $\lambda_\xi$  and  $\lambda_\eta$  are as follows,

$$\begin{aligned} \lambda_\xi &= \bar{q} \cdot \bar{S}_\xi + c |\bar{S}_\xi| \\ \lambda_\eta &= \bar{q} \cdot \bar{S}_\eta + c |\bar{S}_\eta| \end{aligned} \quad (3.21)$$

where,  $\bar{S}_\xi$  and  $\bar{S}_\eta$  are the cell normal vector along each grid line direction,  $\bar{q} = (u, v)$  is the velocity vector and  $c$  is the speed of the sound and  $K_t$  is a constant that has been set to 2.5 based on numerical experiments.

### Residual Smoothing

By using implicit smoothing of the residuals, the stability range and robustness, along with the convergence to steady state of the basic time-stepping scheme can be increased As suggested by Jameson and Baker (1983), the residual smoothing for three-dimensional flow, can be applied in the form,

$$(1 - \beta_\xi \nabla_\xi \Delta_\xi)(1 - \beta_\eta \nabla_\eta \Delta_\eta) \bar{R}_{i,j} = R_{i,j} \quad (3.22)$$

where,  $R_{i,j} = \frac{1}{\Omega} \bar{Q}(U)$  is the original residuals for the explicit time-stepping scheme and  $\bar{R}_{i,j}$  represents the residuals after the sequence of smoothing in  $\xi$  and  $\eta$  directions with the coefficients  $\beta_\xi$  and  $\beta_\eta$ . The residual smoothing is applied in the second and fourth time step of the four-stage Runge-Kutta integration In Eq 3.22, it is necessary to solve a sequence of tridiagonal equations for separate scalar variables. The use of constant coefficients in the implicit treatment has been proven to be beneficial in extending the CFL number to a considerable higher level than that in general used in the basic time stepping scheme without residual smoothing, which enhances the convergence rate quite significantly. This has been quite satisfactory even for highly stretched meshes, provided additional dissipative support such as enthalpy damping is introduced. However, the use of enthalpy damping, which assumes constant total enthalpy throughout the field, precludes the solution of problems with heat transfer effects. Using the above-mentioned can eliminate the need for enthalpy damping variable coefficients  $\beta_\xi$  and  $\beta_\eta$  that account for the variation in cell aspect ratio. For the factorization of Eq 3.22, effective expressions for the coefficients  $\beta_\xi$  and  $\beta_\eta$  can be derived following the procedure of Martinelli (1987), as

$$\begin{aligned} \beta_\xi &= \max \left\{ \frac{1}{4} \left[ \left( \frac{\text{CFL}}{\text{CFL}^*} \frac{\lambda_\xi}{\lambda_\xi + \lambda_\eta} \Phi_\xi \right)^2 - 1 \right], \varepsilon \right\} \\ \beta_\eta &= \max \left\{ \frac{1}{4} \left[ \left( \frac{\text{CFL}}{\text{CFL}^*} \frac{\lambda_\eta}{\lambda_\xi + \lambda_\eta} \Phi_\eta \right)^2 - 1 \right], \varepsilon \right\} \end{aligned} \quad (3.23)$$

where, CFL is the Local Courant Number used in the computational scheme and  $\text{CFL}^*$  is the maximum allowable Local Courant Number based on stability analysis of the explicit Runge-Kutta scheme.  $\Phi_\xi$  and  $\Phi_\eta$  are defined as

$$\Phi_{\xi} = 1 + \left( \frac{\lambda_{\eta}}{\lambda_{\xi}} \right)^{\sigma}$$

$$\Phi_{\eta} = 1 + \left( \frac{\lambda_{\eta}}{\lambda_{\xi}} \right)^{\sigma}$$

where  $\lambda_{\xi}$  and  $\lambda_{\eta}$  are the quantities given by the equation 3.21 and  $\sigma$  has taken to be 2/3 for the two-dimensional simulations. The quantity  $\varepsilon$  used in the above Eqs. 3.22, is used as a limiter. Dimensional analysis carried out found the value of  $\varepsilon$  lying between 0.10 and 0.25. For the present work, a value of 0.12 is used based on numerical experimentation that assures stability along with enhancing the convergence. For the present four-stage scheme,  $CFL = 1.0$  and  $CFL^* = 2.5$  are used.

### 3.4 Closure

The two-dimensional filtered compressible Navier-Stokes equations and the numerical algorithm in discretization of governing equations in the finite volume formulation are presented in this chapter. The numerical procedure, along with the different acceleration techniques such as local time stepping and implicit residual smoothing has been discussed elaborately.

## CHAPTER - 4

### RESULTS AND DISCUSSION

#### 4.1 Introduction

A flow solver has been developed based on the finite volume formulation for compressible flows. The algorithm includes piecewise linear least square reconstruction, the Advective Upstream Splitting Method (AUSM) and a second-order time marching technique. The first section of this chapter deals with the computation of flows for different test cases both for supersonic and subsonic flow regimes, which illustrate the accuracy of the solver. The flows over a 4% thick circular arc bump for different conditions are computed. Another test case is the flow field developed due to shock-boundary layer interaction over a flat plate. As already mentioned, the principal objective of the work is to test the applicability of the flow solver to capture the unsteady flows by Large Eddy Simulation. Thus the second part deals with the computation of the flow over a backward facing step by LES. Considering the time frame, the study is restricted to the two-dimensional analysis.

#### 4.2 The Euler and Navier-Stokes analyses of flow over a 4% thick circular arc bump:

As an illustrative problem, the supersonic and subsonic flows past a 4% thick circular arc bump in a channel are computed. Both the Euler and Navier-Stokes analyses are presented, for the free-stream Mach numbers of  $M_\infty=1.4$  and  $M_\infty=0.5$ . Predicted surface Mach numbers are compared with the previously computed results of Ni (1982).

##### 4.2.1 Grid generation and boundary conditions

The computational mesh for the inviscid calculation consists of  $70 \times 50$  grid points as shown in the Fig. 4.1. The grid is algebraically generated H grid. The corresponding mesh for the viscous calculation is shown in Fig. 4.2. A highly refined stretched grid is used near the upper and lower boundaries for resolving the viscous layers. A grid sensitivity test is conducted for choosing the number of grid points need for the Navier-Stokes solution. The surface Mach numbers for three different grids of sizes  $60 \times 40$ ,  $80 \times 60$  and  $100 \times 80$  are plotted respectively (Fig. 4.3). The surface Mach number obtained from the refined grid  $100 \times 80$  is shown to be almost indistinguishable from that with  $80 \times 60$  grids.

Hence a grid of  $100 \times 80$  is chosen inside the flow domain for the Navier-Stokes calculations

Now, the boundary conditions are described. At the inlet all the variables are imposed for the supersonic flow. For the subsonic inlet, the total pressure and the total temperature are specified and the axial component of the inlet velocity is computed as a part of the solution. At the exit, all the variables are extrapolated for the supersonic flow and the pressure is imposed in case of the subsonic flow. For the Euler solution the normal component of velocity is made to zero at the wall. On the wall, no-slip conditions are imposed for viscous calculation.

#### 4.2.2 Results from the Euler and Navier-Stokes calculations

It has been decided to examine the effect of the higher order discretization of the convective terms. Fig. 4.4, 4.5 and 4.6 illustrate the computed flows over a bump in a channel for supersonic inlet with different orders of spatial discretization. The discretization process has been described in chapter 3. It can be seen that two oblique shocks have formed at both corners of the bump. The leading edge shock is reflected back by the upper wall into the region of expanding flow field. The interaction between the reflected and trailing edge shocks near the trailing edge is captured by the solver, although the accuracy depends on the order of spatial discretization. It is found that the second-order accurate scheme is less dissipative than the first-order. The first-order AUSM is highly dissipative. It has been also seen that there is no significant difference between the solutions obtained from the third- and second-order of the spatial accuracy (Fig. 4.5 and 4.6).

Figure 4.7 demonstrates the comparison of the surface Mach numbers obtained from the Euler solutions where convective terms have been discretised by the first-, second- and third-order upwind schemes. The trend is similar as obtained earlier. There is a significant improvement of the solution when second-order of spatial accuracy for the convective terms has been used. However, the increase in accuracy is very small between the results obtained from the second- and third-order of accurate solutions. Thus the second-order spatial discretization of the convective terms following AUSM will be adopted for further calculations.

Figure 4 8 represents the surface Mach number distribution over the bump placed in a channel with the inlet Mach number of 1.4. The results obtained from the Euler solutions of second-order AUSM is compared with the results presented by Ni (1982). It is evident from the figure that the present calculation is in good agreement with that of Ni. Moreover, the interaction of the reflected and trailing edge shock near the trailing edge of the bump is better resolved here.

So far the results presented were the solution of Euler equations. Now, the Navier-Stokes computation i.e. the viscous calculations over the same bump arc are presented for the free stream Mach number of 1.4.

Figure 4 9 represents the Mach contours for the viscous calculation over the bump for supersonic flow. There is no appreciable difference between the Navier-Stokes and the corresponding Euler solutions (Fig 4 5) except near the trailing edge region of the bump. This is due to the formation of the boundary layer and its interaction with the shock. Here the shock has reflected from the top of the boundary layer. This phenomenon is absent in the Euler solution, where the shock will reflect from the wall. Moreover, the flow may also separates due to the shock-boundary layer interaction. The surface Mach number distributions are plotted in Fig 4 3 for the second-order Navier-Stokes solution. The nature of the curve is same as that of the Euler solution. Thus the present computation indicates that there exists very little difference between the surface pressure predicted by the Euler and the Navier-Stokes equations.

The skin-friction coefficient over the bump is presented in Fig 4 10. It is found that a sudden increase in the skin-friction coefficient occurs at the trailing edge. The increase of the skin-friction occurs due to the acceleration of the flow over the bump, which causes the increase in velocity gradient at the wall. At the trailing edge of the bump the flow meets with the reflected shock which results in sudden decrease of velocity close to the wall. This is the result of the sudden drop of skin-friction at the trailing edge. The flow has a tendency to separate there. The similar trend has been reported by Parthasarathi and Kallinders (1995).

Figure 4 11 indicates the Mach contours obtained from the steady state Euler solution of flow over the bump placed inside a channel for subsonic flow ( $M_\infty=0.5$ ) It has been seen that the Mach contours are quite symmetric over the bump, which indicates the accuracy of the presented computation The surface Mach number distribution has also become symmetric over the bump (Fig 4 12) Both of these results are similar to that of Ni (1982) The corresponding Mach contours over the bump obtained from the viscous calculation at  $M_\infty=0.5$  is illustrated in Fig 4 13 Here the symmetric nature of the Mach contours has lost due to the boundary layer growth as the flow past over the bump However the nature of the surface Mach number distribution remains almost similar to that of the Euler solution as shown in Fig 4 14

#### 4 2 3 Conclusions

The computed results of the Mach contours and the surface pressure distributions both from the Euler and Navier-Stokes equations are presented for the flow over a circular arc bump placed inside a channel The calculations have been made both for subsonic and supersonic flow conditions Predicted results indicate the accuracy of the solver to resolve the flow pattern It should be noted that the second-order accurate AUSM scheme gives accuracy acceptable for engineering applications

### **4.3 The shock-boundary layer interaction over a flat plate**

This section deals with the analysis of the boundary layer separation due to the impingement of a shock wave over a flat plate The results are compared with the available experimental results

#### 4 3 1 Grid generation and the boundary conditions

The grid used for the present study is shown in Fig 4 15 Here also an algebraically generated H grid is chosen with high exponential grid stretching near the wall A flow tangency condition is applied on the upper surface No-slip boundary conditions are imposed at the solid wall The total pressure and the total temperature are specified at the inlet section and the axial component of the inlet velocity is computed as a part of the solution At the outlet all the dependent variables are extrapolated A weak shock is directed towards the boundary layer at an angle  $32.58^\circ$  with the direction parallel to the wall

#### 4.3.2 Analyses of the shock-boundary layer interaction

The schematic view of the shock-boundary layer interaction is shown in Fig 4.16. It can be seen that a shock is formed at the leading edge of the plate. The shock creates an adverse pressure gradient causing the growth of the boundary layer there. The incident shock is directed at a certain angle parallel to the wall. This shock reflects from the top of the boundary layer and an adverse pressure gradient is created. It also results in further growth of boundary layer. The adverse pressure gradient may be strong enough to cause the boundary layer separation. This flow again reattaches the wall downstream of the shock as shown in the figure.

The numerical simulation of the shock-boundary layer interaction problem is performed with  $70 \times 56$  grid points. The Mach contours are presented in Fig 4.17 for free-stream Mach number of 2.0. The incident shock and its reflection from the top of the boundary layer are captured properly by the AUSM algorithm. The shock impingement creates an adverse pressure gradient, which increases the boundary layer thickness. The increase in boundary layer thickness is clearly visible from the Mach contours. The boundary layer growth is also same as that of diagram A. A leading edge shock similar to the schematic diagram is also visible from the figure.

The velocity vectors close to the wall for the flow are depicted in Fig 4.17. It is found that the adverse pressure gradient due to the incident shock not only thickens the boundary layer but also results in the separation of flow. The separation, recirculation and the reattachment of flow are clearly illustrated by the computed velocity field.

The skin-friction coefficient is plotted in Fig 4.18. The negative value of the skin-friction coefficient further justifies that the separation of flow occurs where the shock meets with the boundary layer. The result is verified with the experimental data by Hakkinen et al (1959). From this comparison, it is inferred that the AUSM under predicts the skin-friction coefficient in the separation region. Outside this region the computed skin-friction matches reasonably well with the experimental data.

### 4.3.3 Conclusions

The analysis indicates that the solver developed is accurate enough to resolve the complex flow field involving shock-boundary layer interactions and flow separation

## 4.4 Two-dimensional analyses of flow over the backward facing step

The upwind scheme can resolve flow structure well as it is based on the physics of flow. Various upwind schemes have been developed for LES of compressible flows. An attempt is made to simulate the unsteady turbulent flow by using such an algorithm named as AUSM. It has been decided to explore the possibility to apply the scheme for IFS. The flow over a backward facing step with 8:9 expansion ratio is chosen as a test case for IFS computation. However, the free-stream Mach number was very low  $M_\infty = 0.128$ . This was chosen because of the fact that the experimental data for the unsteady flows with turbulence quantities were available to us for this case.

### 4.4.1 Grid generation and the boundary conditions

The length along the streamwise direction of the computational domain that is used for LES calculation is chosen from a trial steady state Navier-Stokes solution. The separation region of flow has found to be confined within an approximate length of  $7H$  downstream of the step (where,  $H$  is the step height). A length of  $16H$  along the streamwise direction after the step is considered to be sufficient for this LES calculation. The height of the computational domain is taken as  $9H$  that equal to the height of the test section. A length of  $8H$  is taken ahead of the step to match the computed boundary layer with that of experimental value before the step. The region is divided into algebraically generated non-uniform computational mesh of size  $100 \times 100$  in the  $x$  and  $y$  directions. The grid is clustered near all the solid boundaries to capture steep gradients of the flow variables near the wall. The computation domain and the grid are shown in Fig. 4.19. The grid is so chosen that the non-dimensional normal distance ( $y^+$ ) maintained of the order of unity near the wall. A relatively high stretching of meshes near the step along the axial direction is chosen to predict the vortex structure generated inside the separation region. A relatively coarse non-uniform mesh spacing is used outside these regions.

A very low inlet Mach number turbulent flow ( $M_\infty=0.128$  and  $Re_H=3.1 \times 10^5$ ) is simulated in this problem. At inlet as the boundary layer thickness is known the boundary layer profile is specified considering 1/7 power law. The static temperature is specified for free stream condition. The density is extrapolated at the inlet plane after each time step. The static pressure is calculated from this density. At the exit plane the static pressure is imposed and all the other flow variables are extrapolated. At the upper and lower walls no-slip boundary conditions are imposed along with a vanishingly normal temperature gradient. The pressure at the solid surface is extrapolated from the interior boundary cell.

#### 4.4.2 Analyses of flow over the backward facing step

The solver is first allowed to run for laminar flow with the same number of grid points and above-mentioned boundary conditions. The steady flow field generated is assumed as initial flow field for LES calculation. Now, the SGS model is turned on for the rest of the simulation, which are continued upto  $10.5 \times 10^5$  iterations. A CFL number of 1.0 is chosen for the entire simulation. The lowest possible time step within the computational domain is used for this simulation. The time step is found to be very small, which needs about  $10^5$  iterations to complete one eddy turn over time (Table 1). The very low free stream Mach number forces to fix time step to a small limit from stability criterion. Thus, only 10 samples have been collected for processing the results. Thus the time-averaged results may not properly match with the available experimental data due to the small number of collected dataset. The simulation is performed in a Pentium III machine with a clock speed of 800 MHz. The computational time needed to complete  $10^6$  iterations is about 130 hours.

Table 1

List of flow Variables	Values
Free-stream Mach number ( $M_\infty$ )	0.128
Average stream-wise velocity ( $V_{avg}$ )	44.2 m/sec
Step height (H)	0.0127 m

List of flow Variables	Values
Eddy turn-over time ( $H u_t$ )	$7.9 \times 10^{-3}$ sec
Time step size ( $\Delta t$ )	$7.4 \times 10^{-8}$ sec

Instantaneous streamlines and vorticity fields are presented at different instants of time as shown in Fig. 4.20 (a-i) and 4.21 (a-d). The complex flow structure, formation and shedding of vortices and its dynamics are well resolved. As the expansion ratio is very small there is no visible vortex formation on the upper wall. The instantaneous flow pattern indicates that the flow field is unsteady.

The accuracy of results can be verified by comparing the time-averaged quantities with the experimental results Driver and Seegmiller (1985). Time averaged streamwise and cross-streamwise components of velocities are compared at 5 different locations as shown in Fig. 4.22. The measurements at station 'a' ( $x/H=-2.0$ ) give the initial value of the velocity fields. The station 'b' ( $x/H=1.5$ ), station 'c' ( $x/H=4.0$ ) provide the velocity fields at the beginning and middle of the recirculation zone. The station 'd' indicates the section where the time-averaged recirculation zone reattaches. In station 'e' ( $x/H=12.0$ ) the velocity profiles are found to be fully developed. It should be noticed that there exist discrepancies between the computed and the experimental results particularly for cross-stream components inside the recirculation zone (at  $x/H=1.5$  and  $x/H=4.0$ ). In the other sections the velocity profiles match more or less correctly with the experimental results. Similar trend was reported by P. Sagaut et al (1994). However they concluded that these discrepancies could be minimized by using a dynamic subgrid scale model where the Smagorinsky constant automatically adjusts itself within the flow field.

Profiles of stream-wise ( $u_{rms}/U$ ) and cross-streamwise ( $v_{rms}/U$ ) turbulence intensities and the mean Reynolds stress ( $\overline{u'v'}/U^2$ ) are plotted at different locations ( $x/H=1.5$ ,  $x/H=4.0$ ,  $x/H=5.5$  and  $x/H=12.0$ ) as shown in Fig. 4.23. It should be noted that the location 'a' and 'b' are inside the separation region. The section 'c' is just outside the recirculation zone and section 'd' is the region where the flow becomes fully developed. All these turbulent quantities as shown in Fig. 4.23 are averaged in both space (filtered) and time. It can be

seen that the present computation is able to capture the existence of a peak of turbulence intensities corresponding to the existence of a spatially evolving mixing layer issued from the separation region although there are some discrepancies. The anomalous peaks near the solid walls have been resulted due to the two-dimensional nature of the flow. The two-dimensional simulation can not predict vortex structure properly. Similar trend was reported by P. Sagaut et al (1994). Moreover, the small number of data sets used for time averaging of the flow variables enhances the error in the results.

An important parameter of the backward facing step flow is the time averaged recirculation zone length. This length can be calculated from the skin-friction coefficient. The reattachment length is equal to the distance from the edge of the step to the point where the value of the coefficient changes from negative to positive. The calculated value of this length is about 5.1 times the step height whereas the experimental value is 6.26 times the step height. Thus, the simulation with the SGS model leads to the severe underprediction of this quantity.

#### 4.4.3 Conclusions

From the above analyses it can be concluded that the Large-eddy simulation by using AUSM algorithm can be able to predict the turbulent flow over the backward facing step. It has been seen that the Smagorinsky model is moderately accurate to calculate the turbulent stresses inside the flow domain. However, for firm conclusion, it should be extended to three-dimensional simulation.

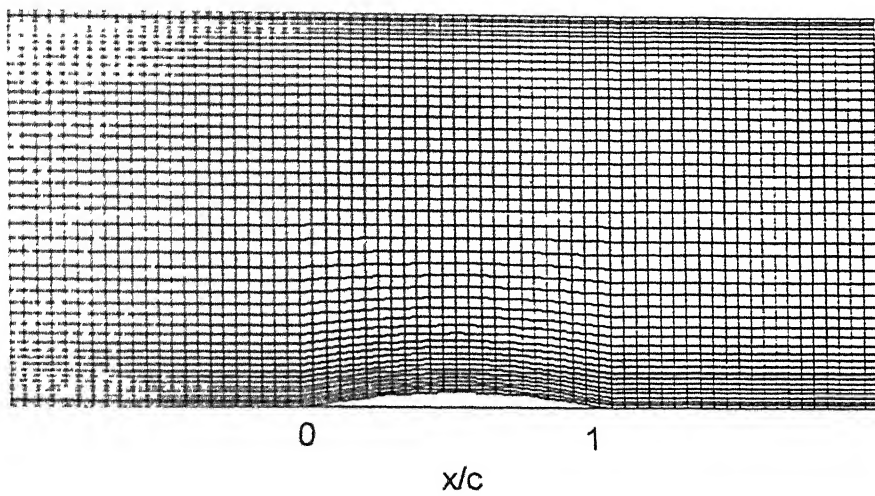


Fig 4.1 Computational mesh for the channel flow with a 4% thick circular arc bump for the Euler calculation

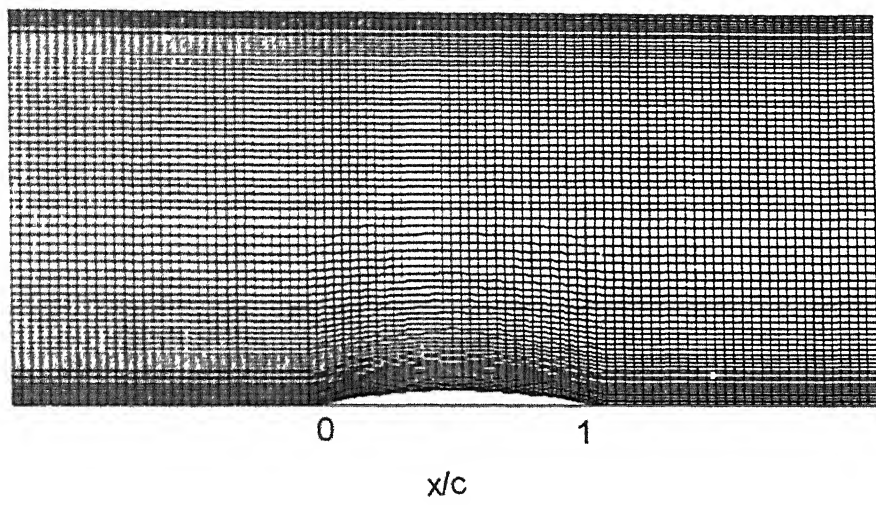


Fig 4.2 Computational mesh for the channel flow with a 4% thick circular-arc bump for the Navier-Stokes solution

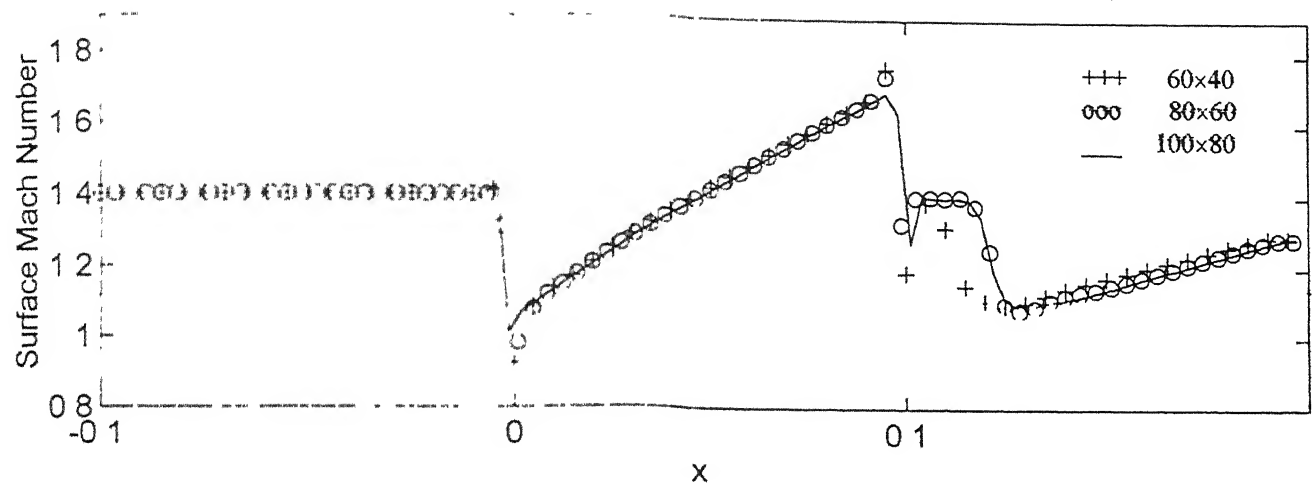


Fig. 4.3 Effect of grid refinement of the surface Mach number distribution for the Navier Stokes solution.

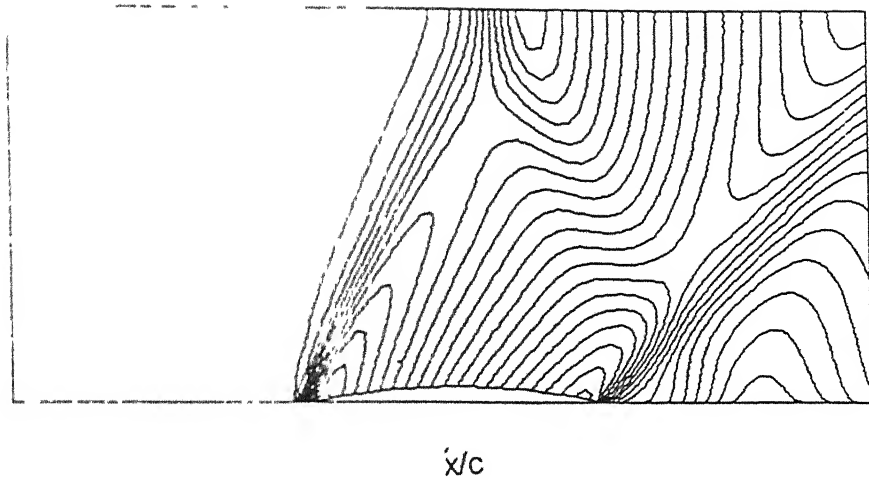


Fig. 4.4 Mach contours for first order Euler solution of supersonic flow in a channel with a 4% thick circular arc bump,  $M_\infty=1.4$ .

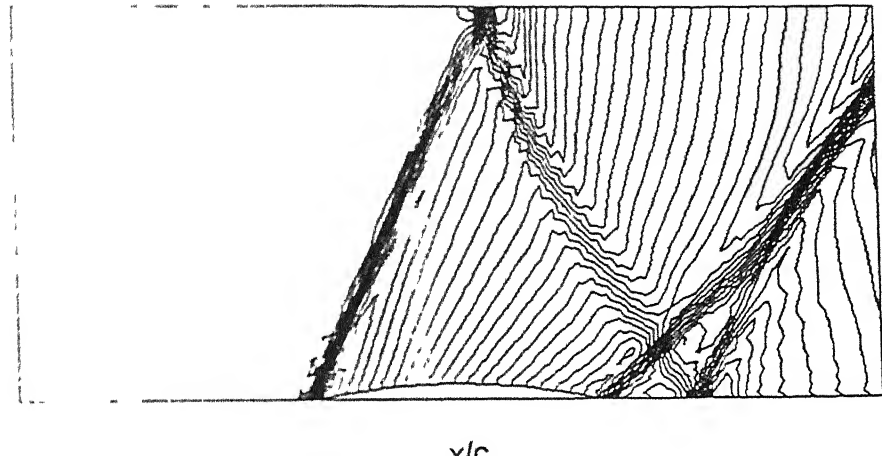


Fig. 4.5 Mach contours for second order Euler solution of supersonic flow in a channel with a 4% thick circular arc bump,  $M_\infty=1.4$

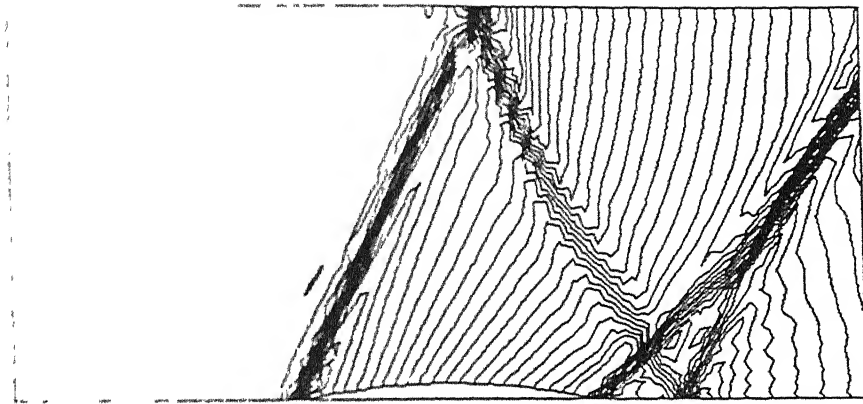


Fig. 4.6 Mach contours for third order Euler solution of supersonic flow in a channel  
with a 4% thick circular arc bump,  $M_\infty=1.4$

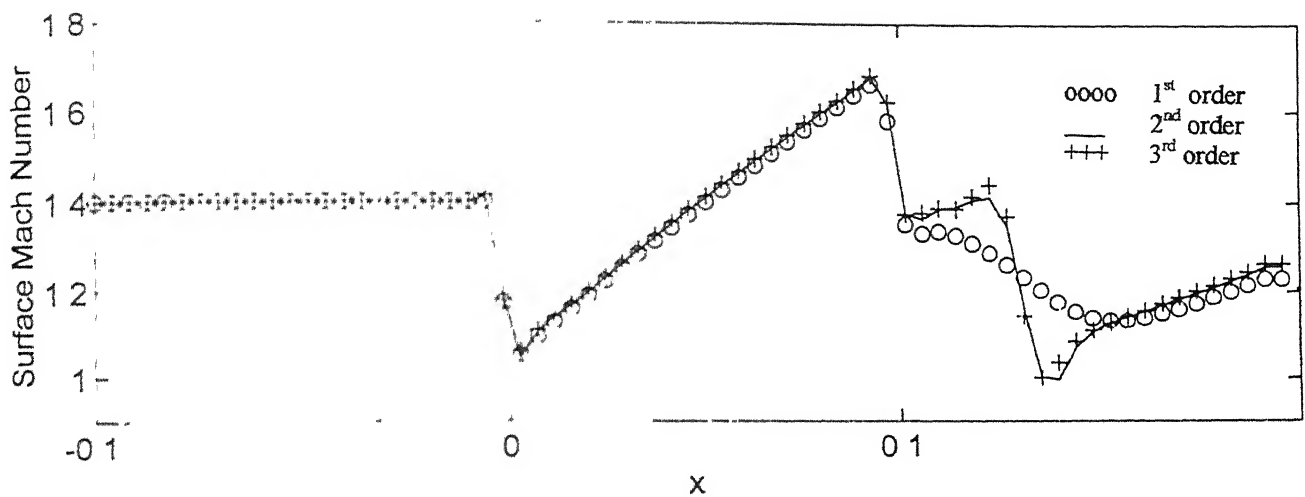


Fig. 4.7 Comparison of surface Mach number distribution between the first, second and third order accurate results over the circular arc bump.

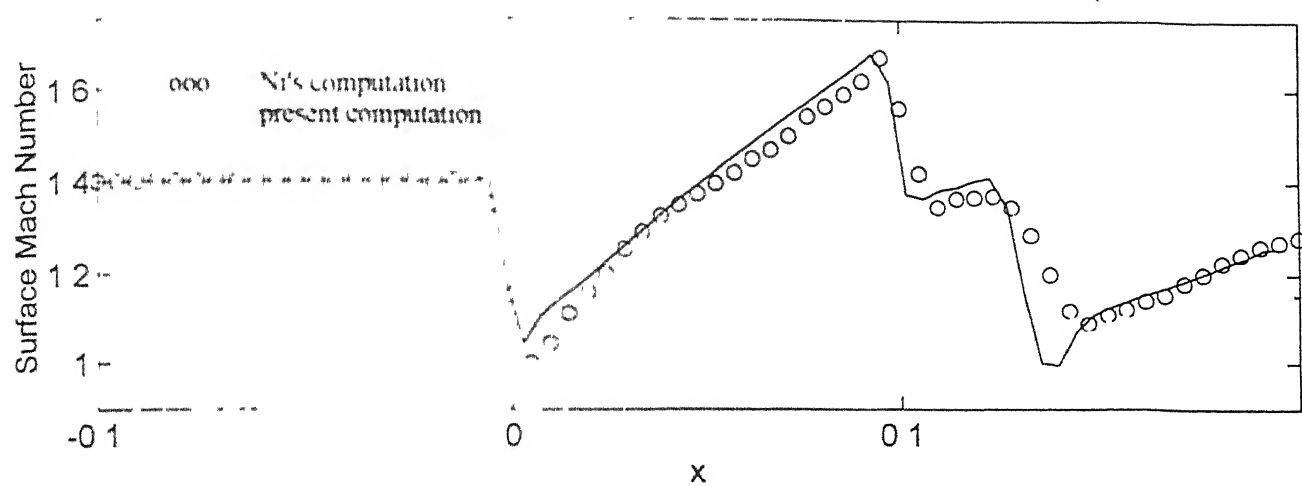
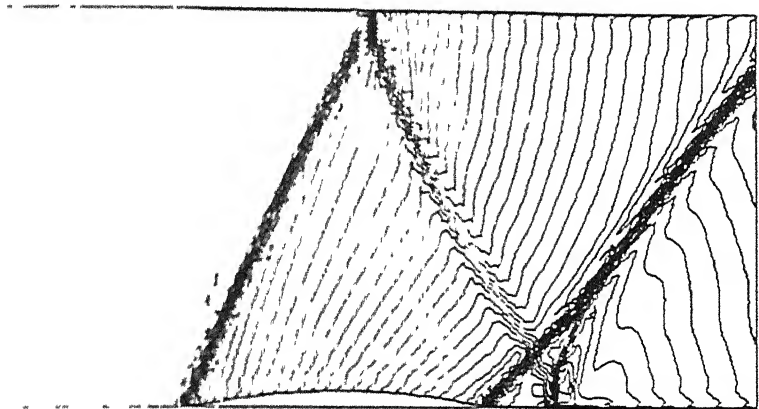
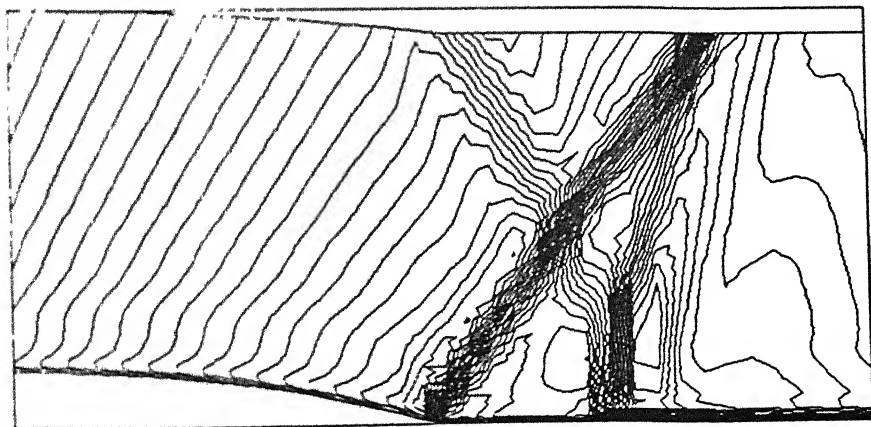


Fig. 4.8 Comparison of surface Mach number distribution for the circular arc bump from Euler solution with the computed results of Ni [1982]



(a)



(b)

Fig. 4.9 Mach contours for Navier-Stokes solution over the 4% thick circular arc bump

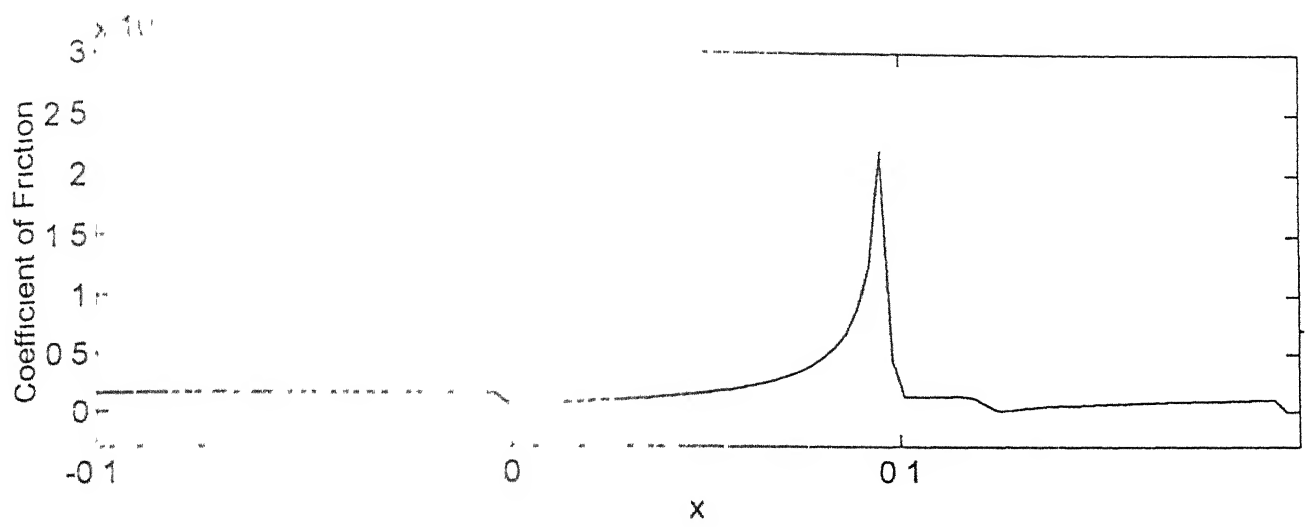


Fig. 4.10 Skin-friction coefficient with  $M_\infty=1.4$  over 4% thick circular arc bump.

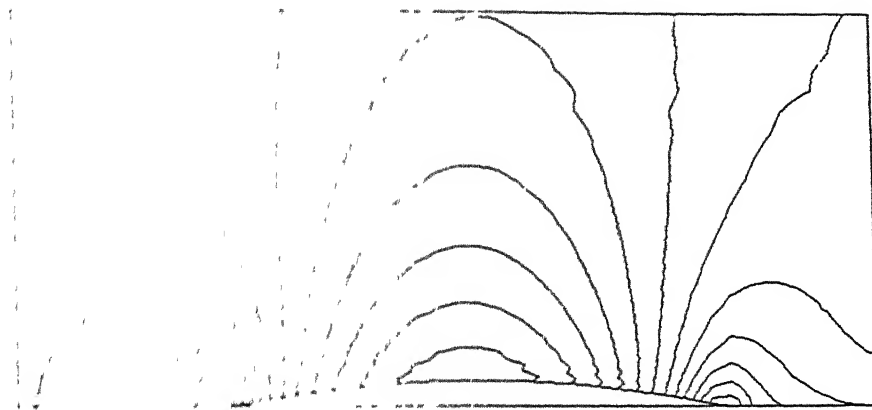


Fig. 4.11 Mach contours for Euler solution of subsonic flow ( $M_\infty = 0.5$ ) over 4% thick circular arc bump

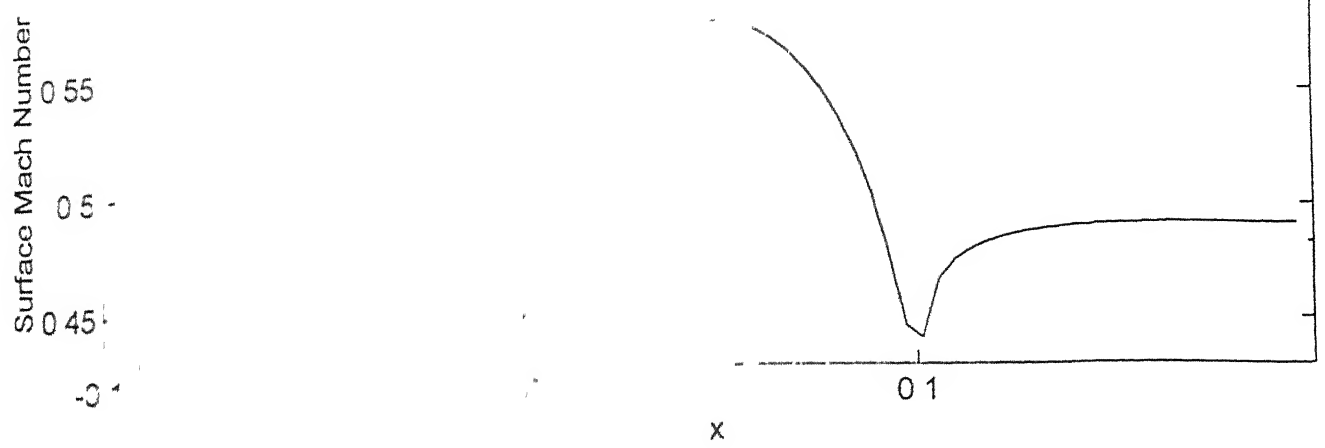


Fig. 4.1. Surface Mach number distribution over a circular arc bump from Euler solution  
 $\alpha_1 = 1.0$

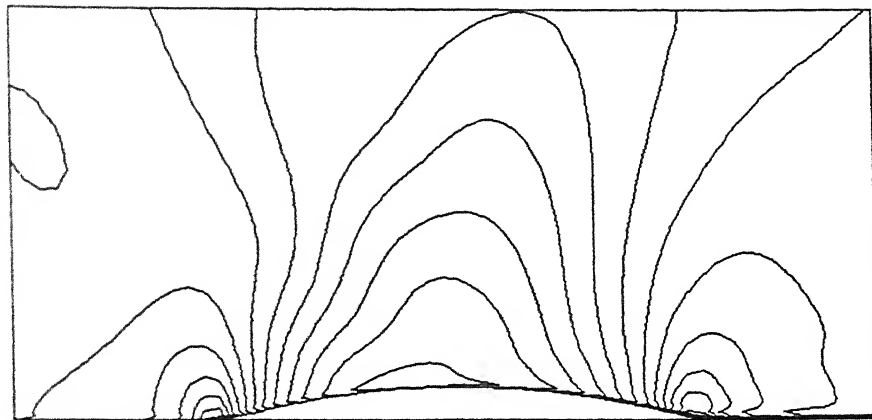


Fig. 4.13 Mach contours of subsonic flow ( $M_{\infty} = 0.5$ ) over a 4% thick circular arc bump

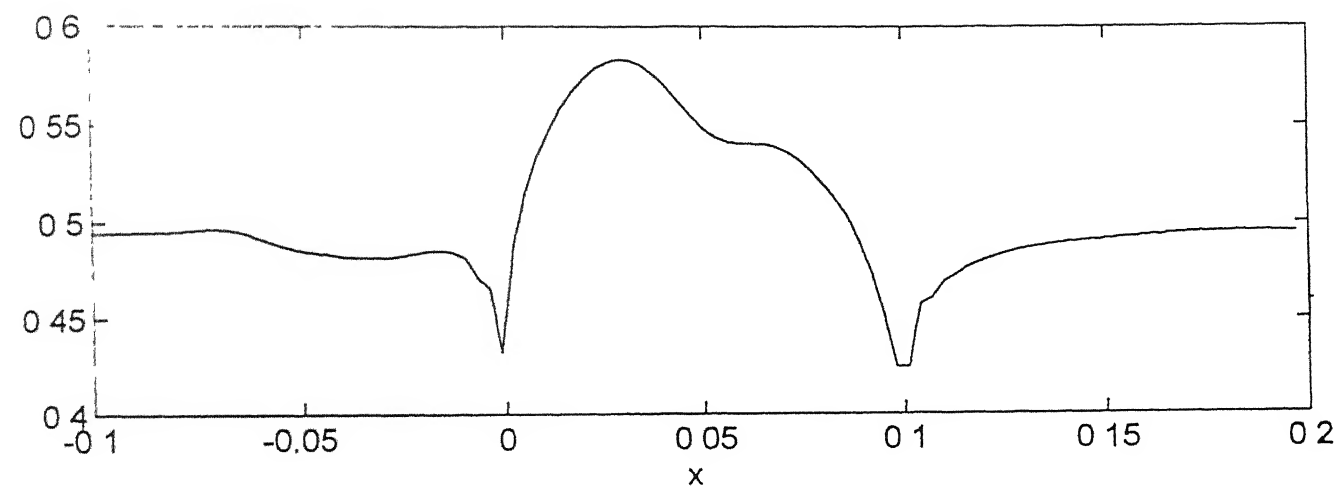


Fig. 4.14 Surface Mach number distribution over a circular arc bump from Navier-Stokes solution with  $M_\infty = 0.5$

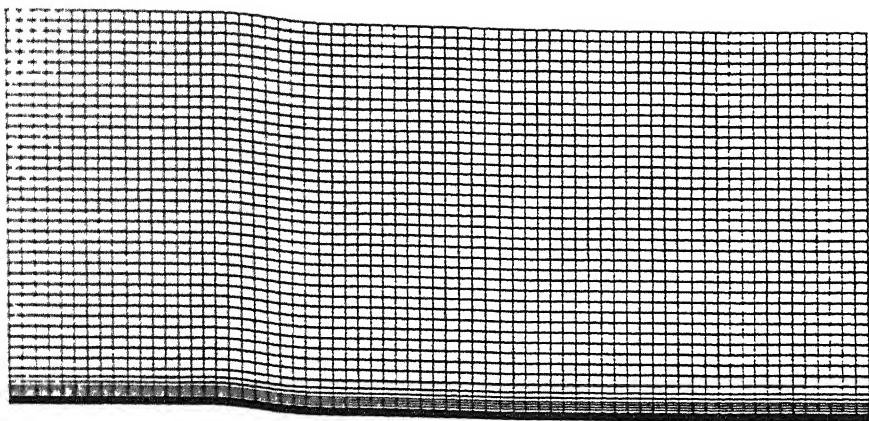


Fig 4.15 Computational mesh over the flat plate for shock-boundary layer interaction problem

ଶ୍ରୀ ପାତ୍ର ସାହେବ

୧୯୮

123643

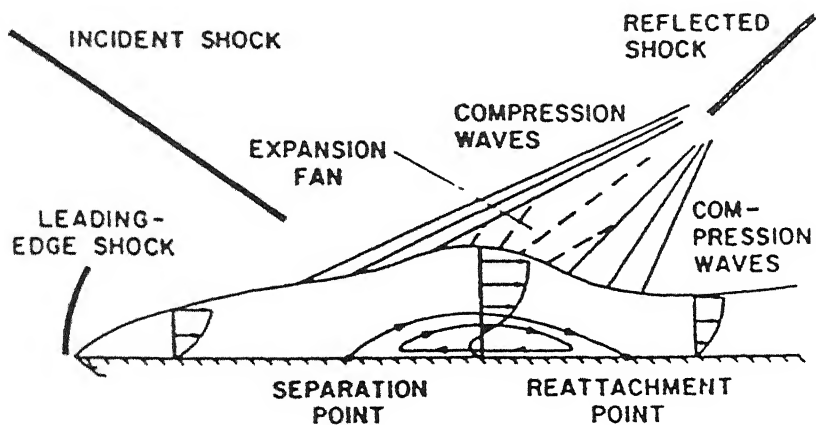


Fig. 4.16 Schematic view of the shock-boundary layer interaction

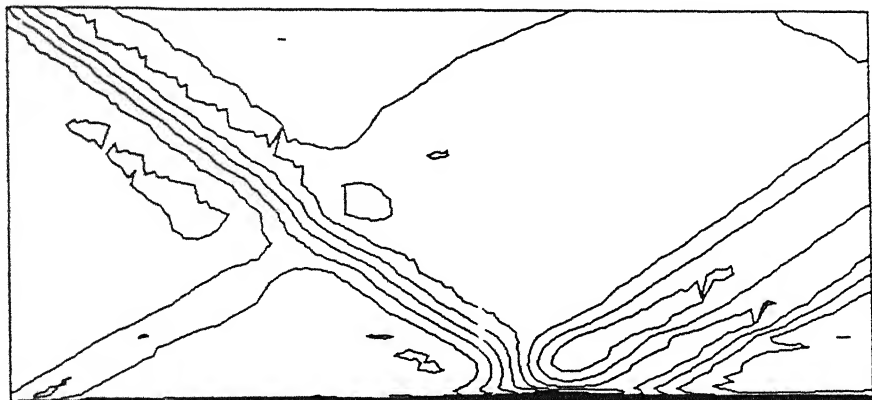


Fig 4 17 Mach contours for shock wave and boundary layer interaction

Experimental	Prediction
Ooooo	—

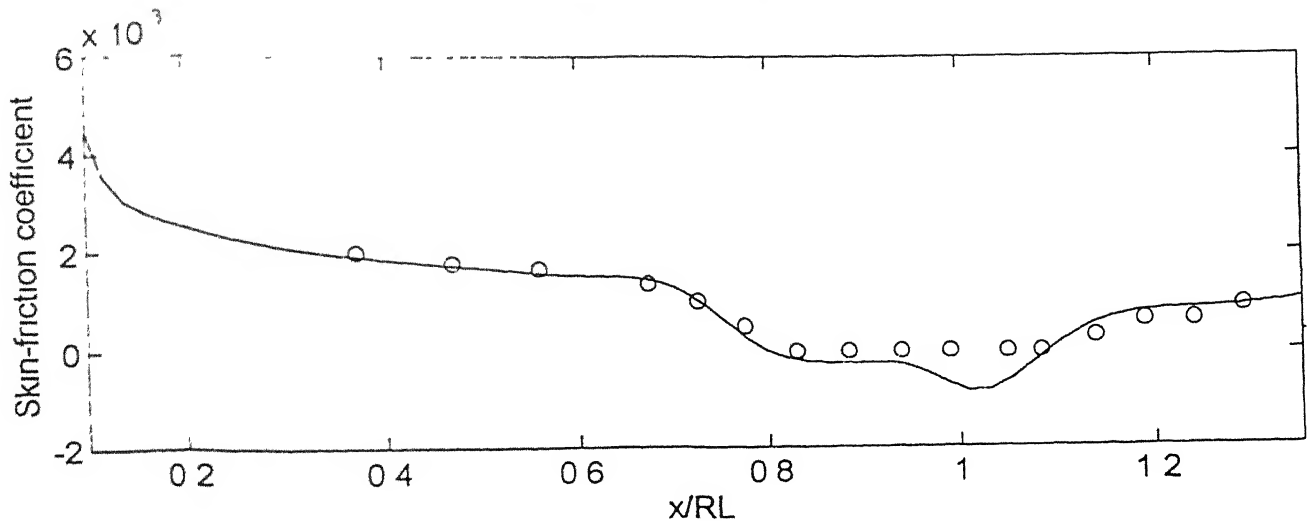


Fig 4.18 Comparison of skin friction coefficient between the experimental and the predicted value for the shock boundary layer interaction problem

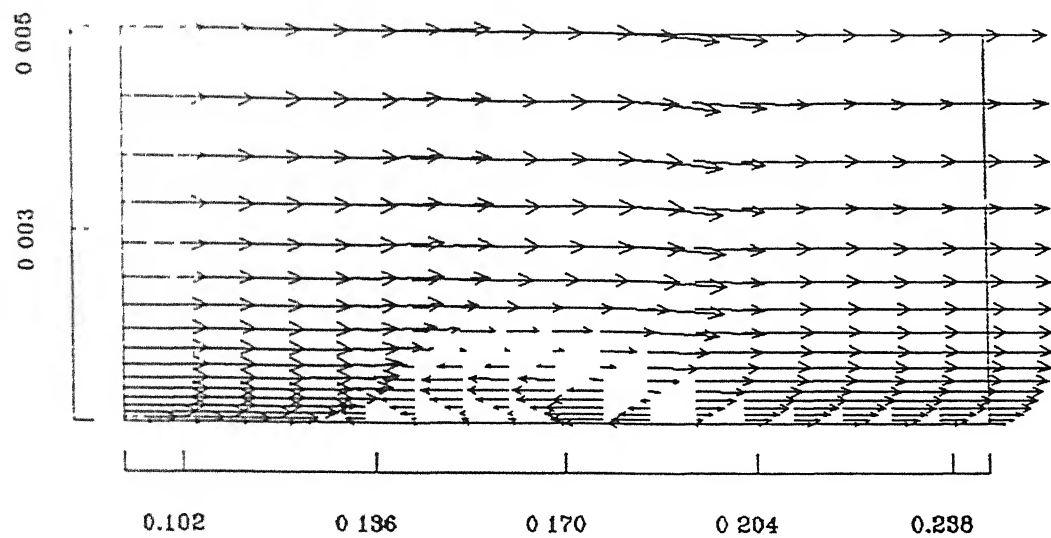


Fig. 4.19 Effect of shock wave on the boundary layer of supersonic flow

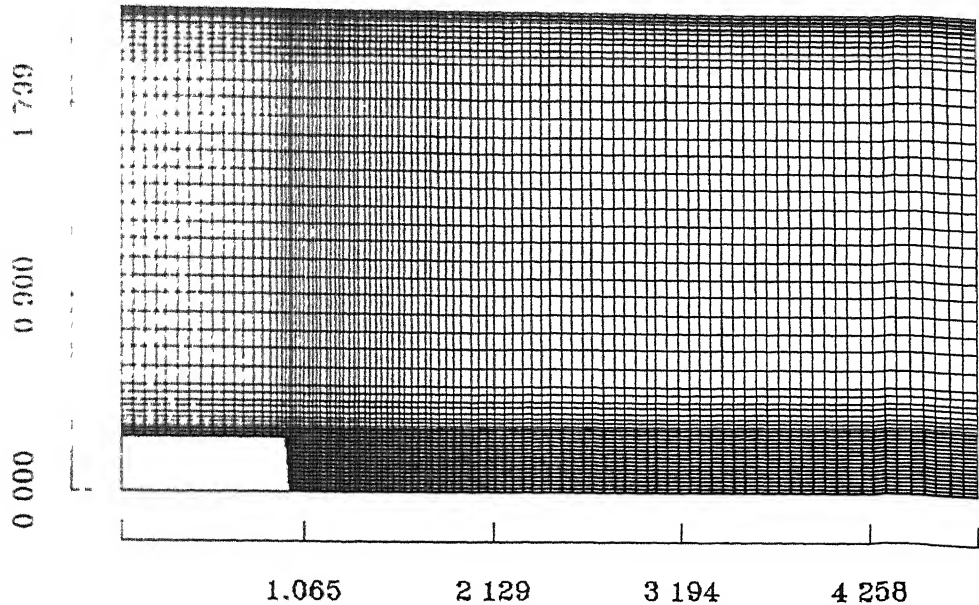
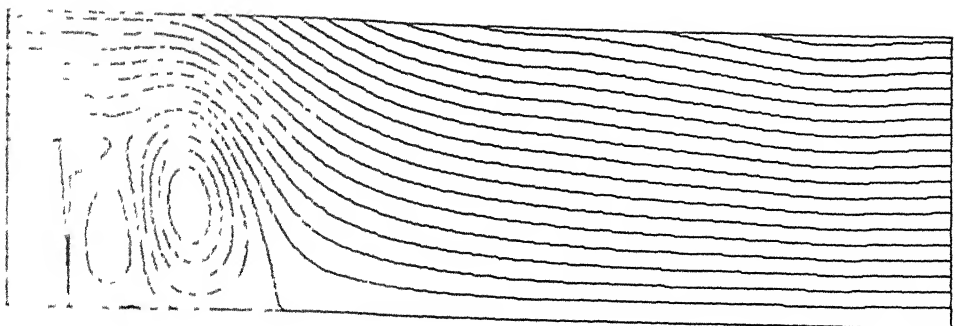
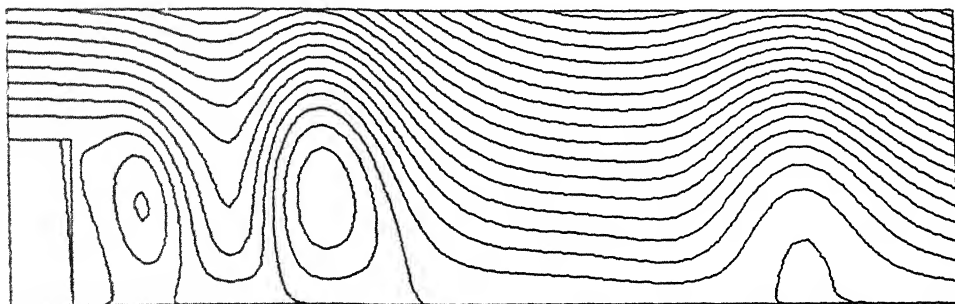


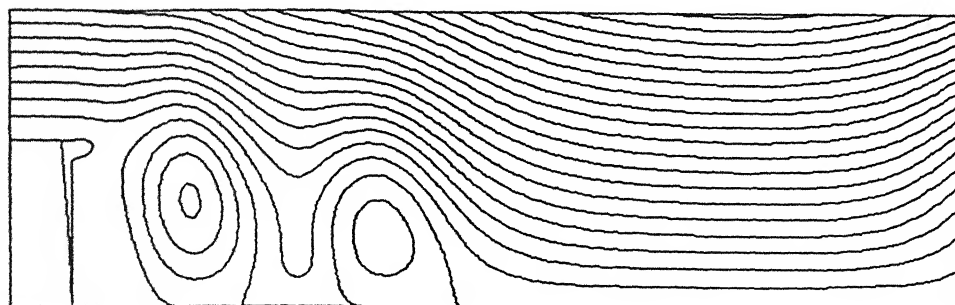
Fig. 4 20 Grid over the backward facing step



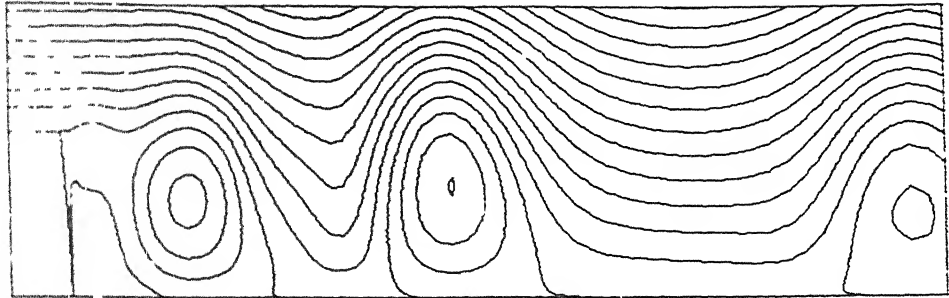
(a)



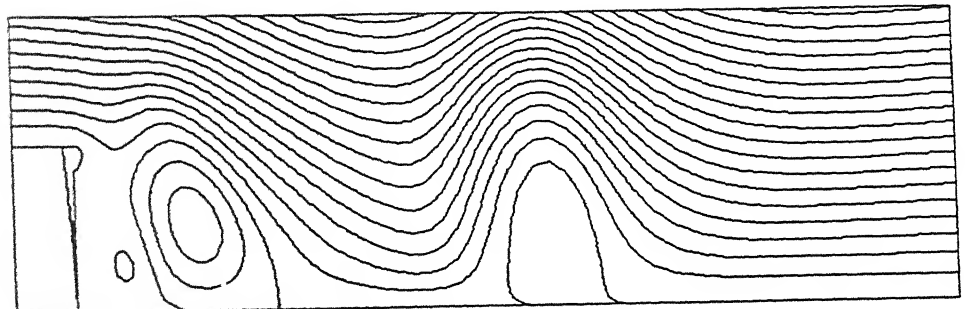
(b)



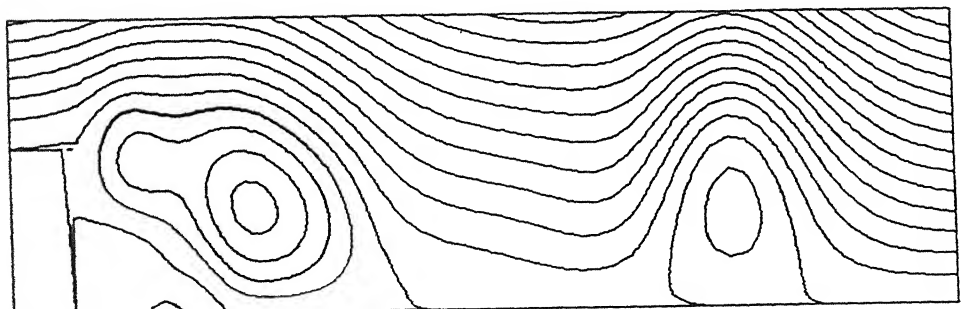
(c)



(g)

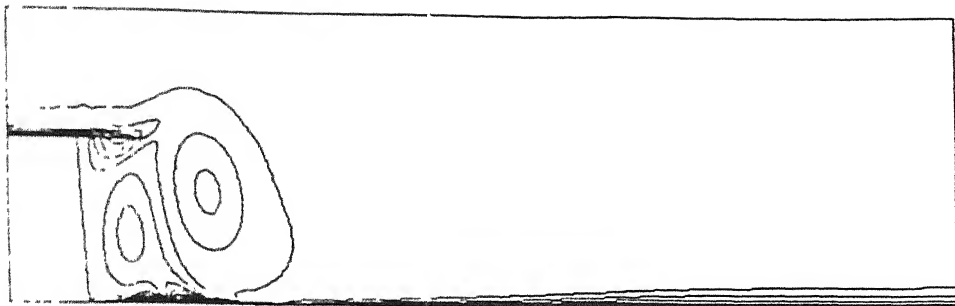


(h)

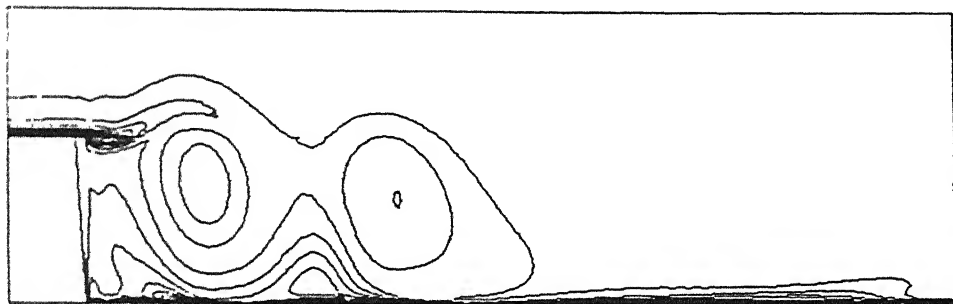


(i)

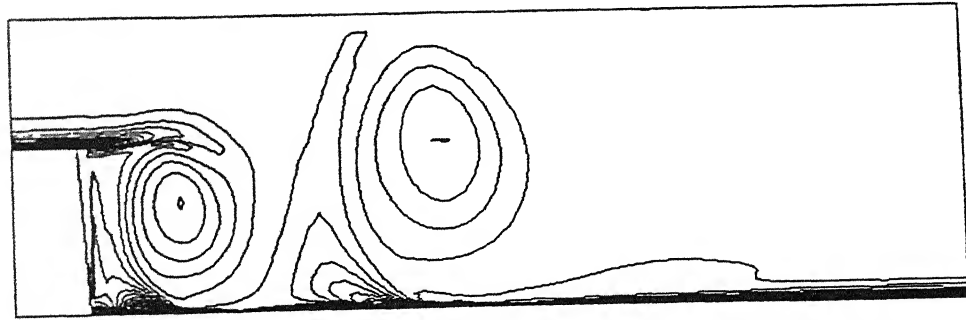
Fig 4.21 Stream function plots at different instant of time downstream of the backward facing step.



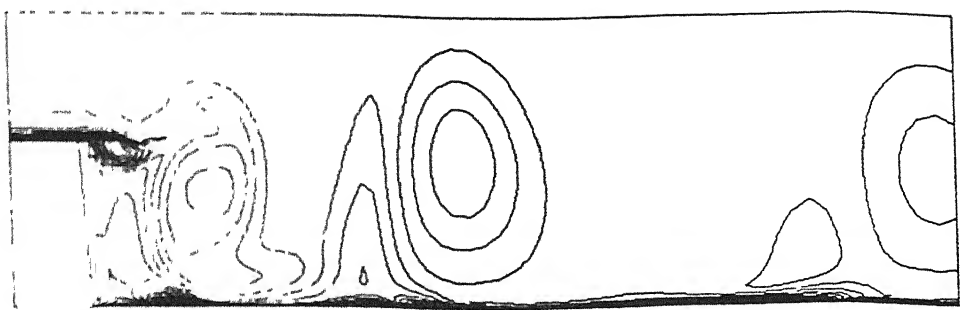
(a)



(b)



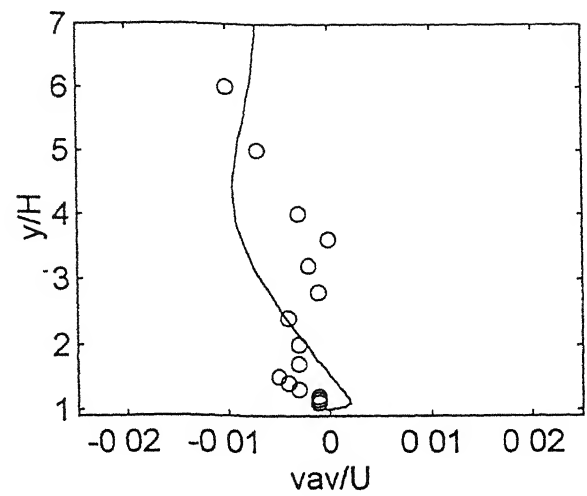
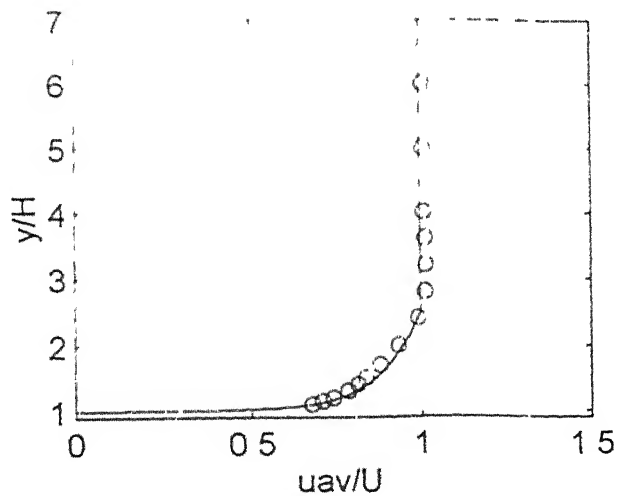
(c)



(d)

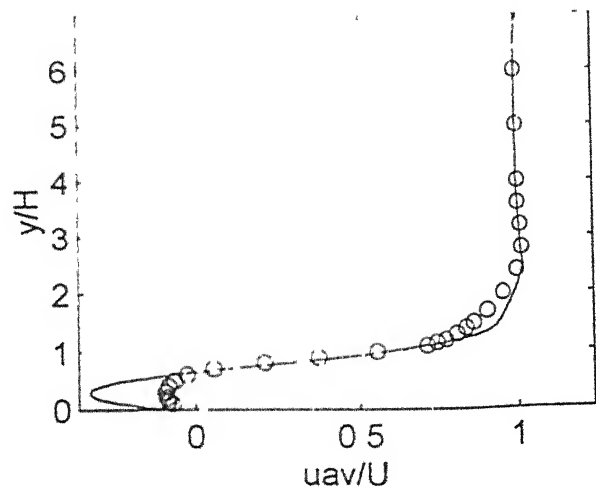
Fig. 4.22 Vorticity plots at different instant of time downstream of the backward facing step

Experimental	Prediction
Ooooo	-----

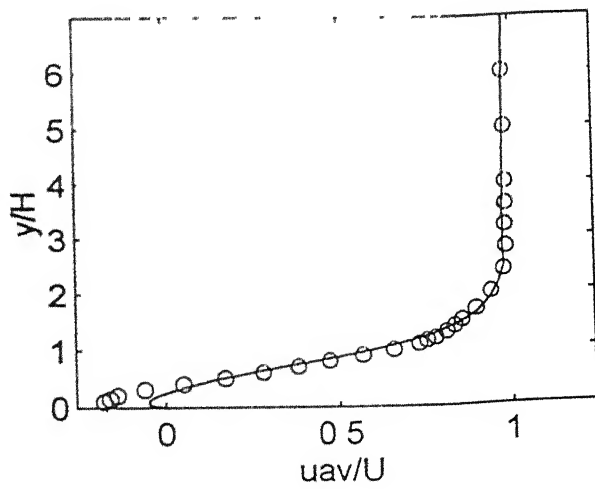
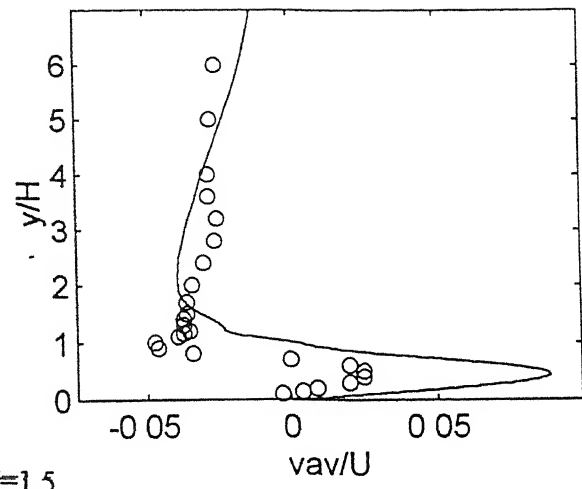


(a)  $x/H = -2.0$

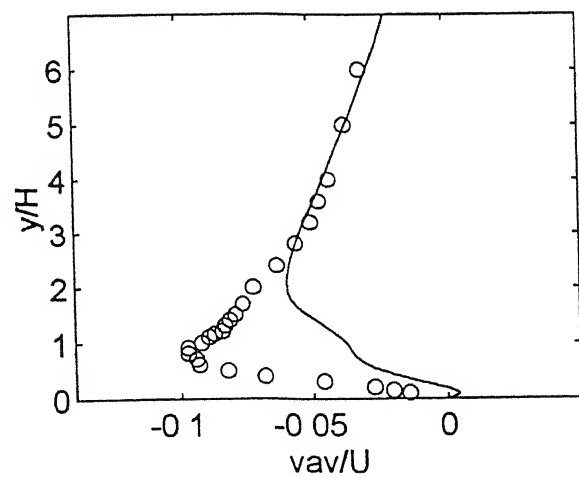
Experimental	Prediction
Ooooo	—



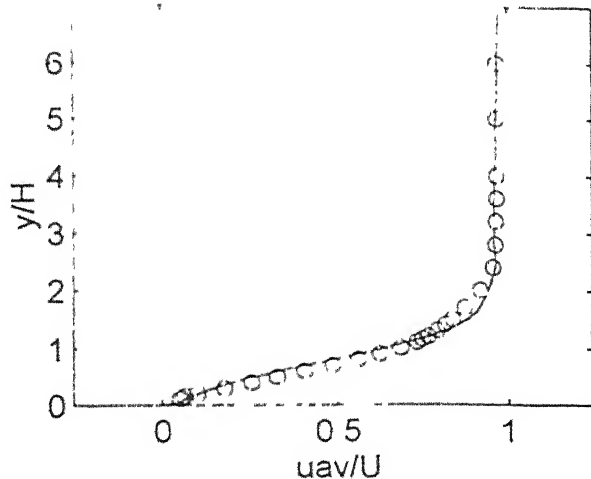
(b)  $x/H=1.5$



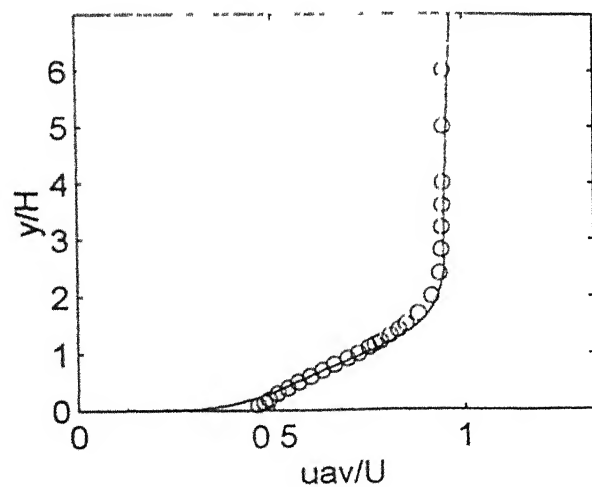
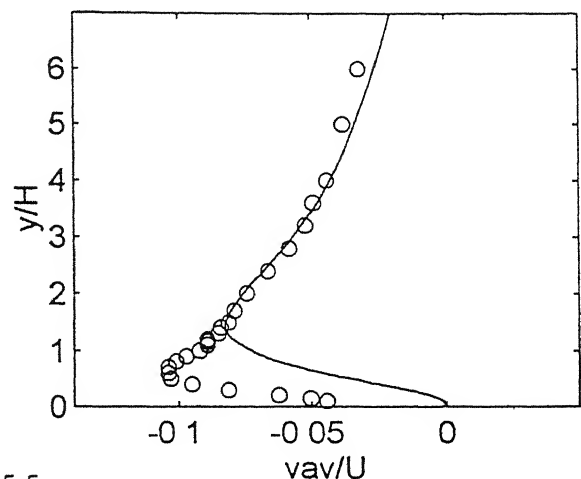
(c)  $x/H=4.0$



Experimental	Prediction
Ooooo	-----



(d)  $x/H=5.5$



(e)  $x/H=12.0$

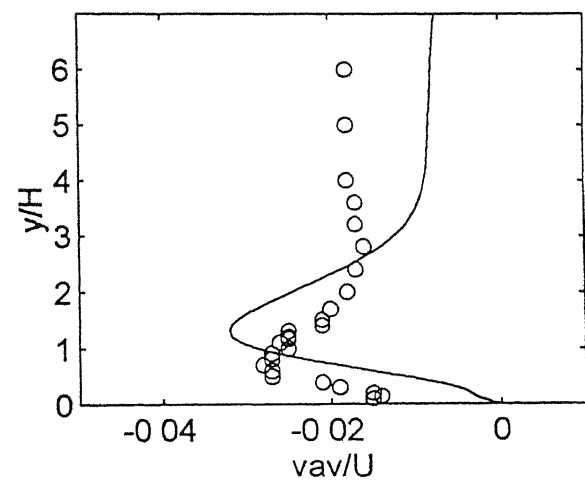
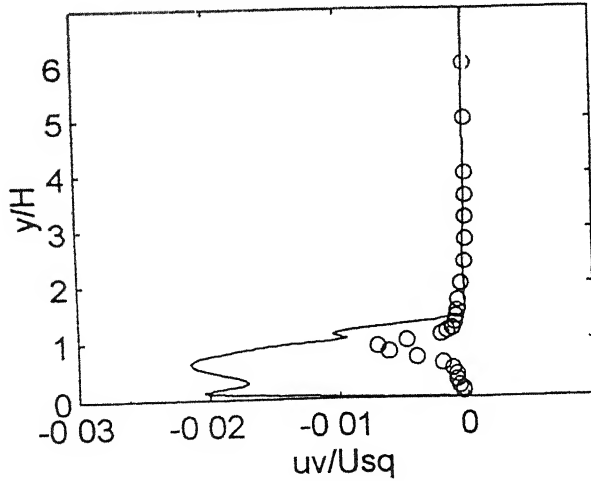
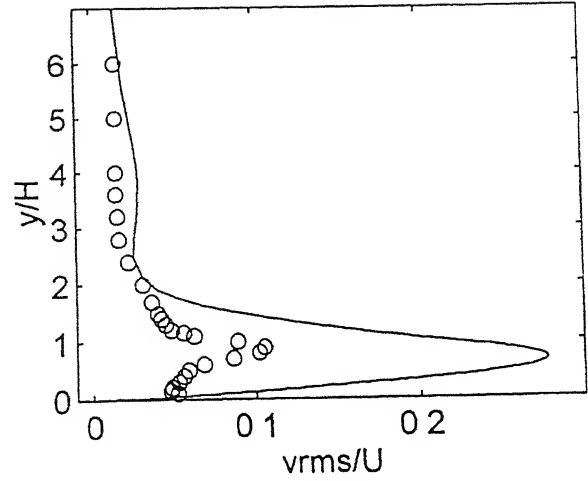
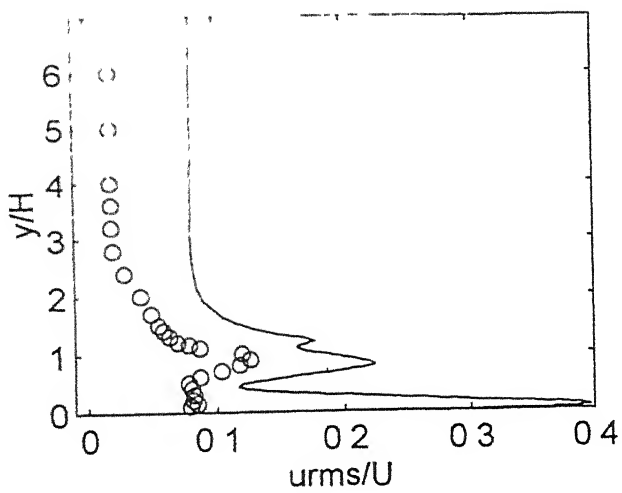


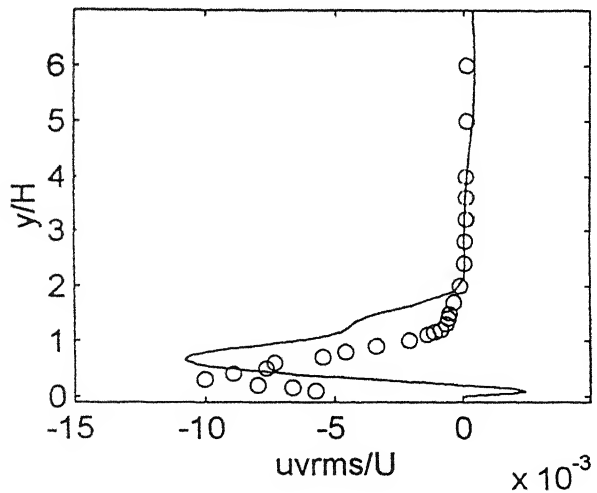
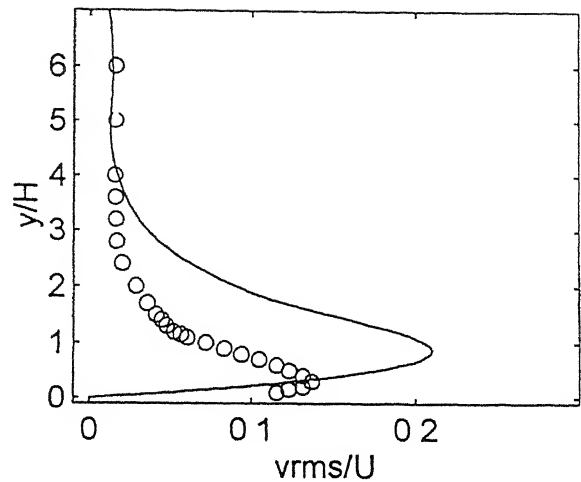
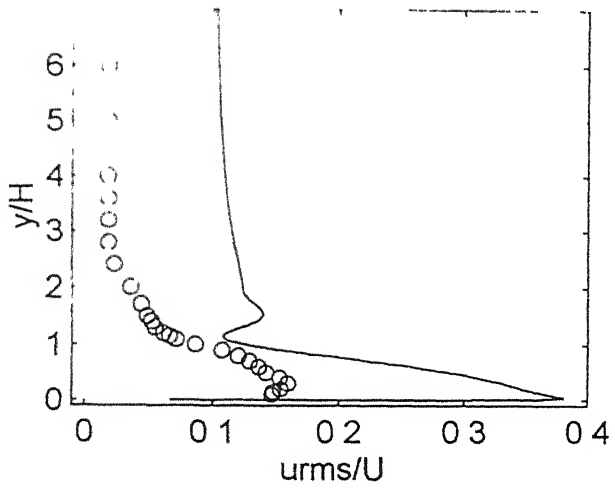
Fig 4 23 Average streamwise and cross-streamwise components of velocity

Experimental	Prediction
Ooooo	_____



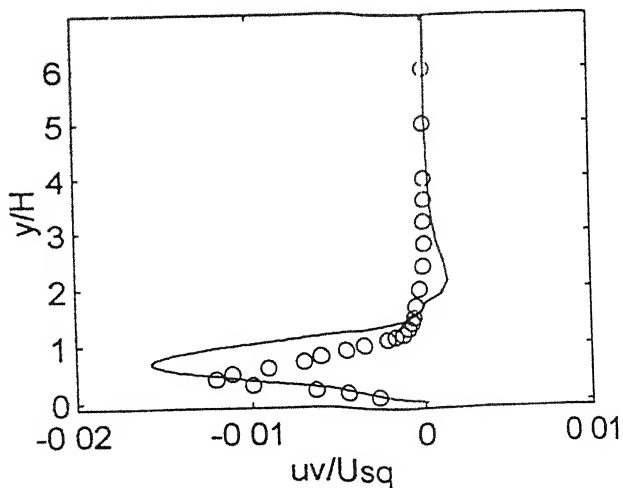
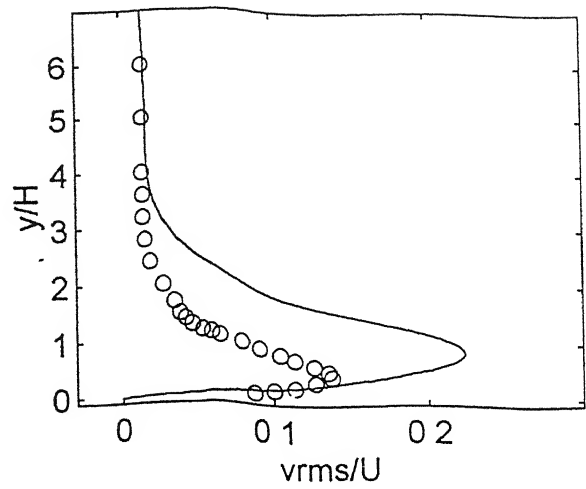
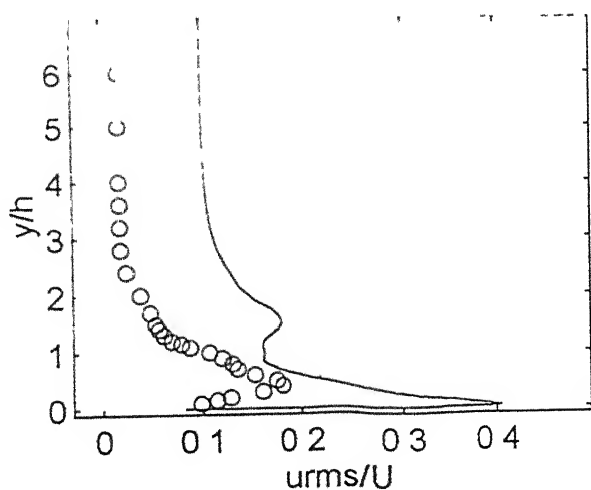
(b)  $x/H=1.5$

Experimental	Prediction
Ooooo	-----



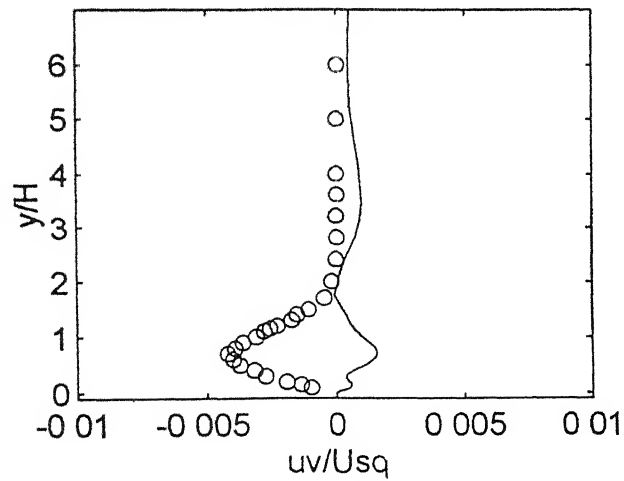
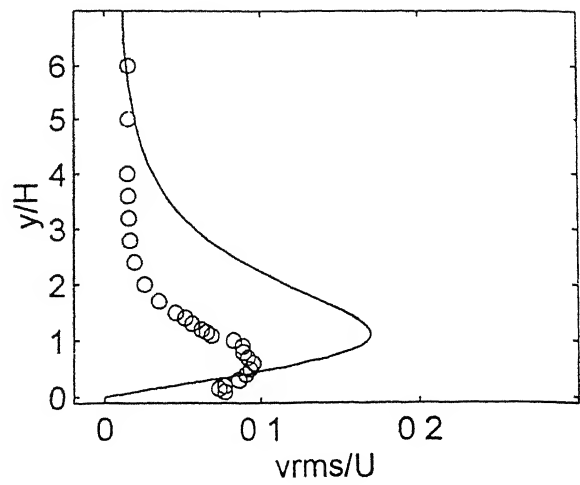
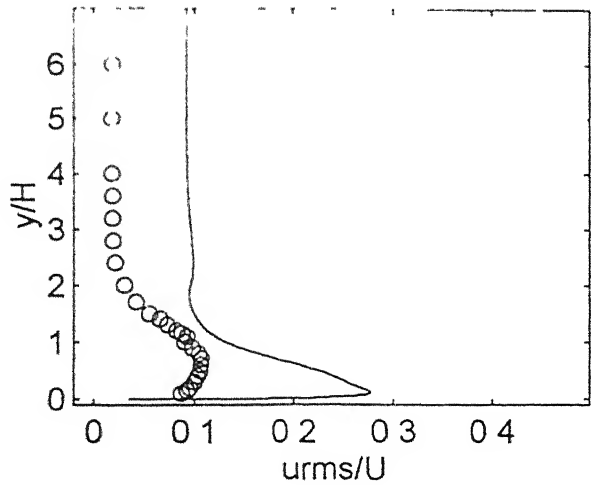
(c)  $x/H=4.0$

Experimental	Prediction
Ooooo	_____



(d)  $x/H=5.5$

Experimental	Prediction
Ooooo	-----



(e)  $x/H=12.0$

Fig 4 24 Average turbulent intensities

## CHAPTER – 5

### CONCLUSIONS

#### 5.1 Conclusions

A two-dimensional flow solver is developed in physical plane using AUSM algorithm to split the convective fluxes. A least square minimization procedure is adopted to define the fluxes at the cell faces. Higher order spatial discretization is made considering the neighbouring cells. The time integration is performed by Runge-Kutta algorithm. The local time stepping and implicit residual smoothing are used to accelerate the steady state solution. The scheme is second order accurate in time and space. For unsteady calculation a global minimum time step is used. At present the calculation is limited to the two-dimensional simulation.

A number of test cases performed illustrate that the solver is reasonably accurate to simulate the complex flow pattern for a widely varying flow conditions from the subsonic to the supersonic flow regime. Finally an attempt is made to simulate the turbulent flow structure over a backward facing step by LES using the flow solver. A simplified SGS model as the Smagorinsky SGS model is used to model the subgrid scale turbulence. It has been found that the solver is able to resolve the unsteady vortex structures generated down-stream of the step. There are some discrepancies between the time-averaged computed and the experimental results. The reasons are for two-dimensional simulation and also for the low number of computed data sets used to generate time-averaged results. Time limitation of an M Tech thesis would not allow the investigator to proceed more. However, with computed results, it can be concluded that the present algorithm may be used to compute practical flows by LES.

#### 5.2 Suggestions for Future Work

The present Large Eddy Simulation has been performed over a backward facing step with two-dimensional formulation. The two-dimensional simulation can not predict the vortex structure properly. The analyses can be extended to three-dimension so as to capture the proper vortex stretching generated downstream of the step. As it has been found that the Smagorinsky model leads to high dissipation a dynamic model may be adopted to model the

subgrid scale turbulence. Finally the solver may be used to simulate very high Mach number flows where gradient limiters should be adopted for stability restrictions.

## References

- 1) Akselvoll, K , and Moin, P , "Large-Eddy Simulation of a Backward Facing Step Flow," Engineering Turbulence Modelling and Experiments 2, Elsevier, pp 303-313, 1993
- 2) Andren, A , Brown, A , Mason, P J , Graf, J , Schumann, U , Moeng, C H and Nieuwstadt, F T M , " A Neutral Stratified Boundary-Layer A Comparison of Four Large-Eddy Simulation Codes," Proc Of the First ERCOFTAC Workshop on DNS and LES, Guildford, Surrey, U K , Kluwer Academic Publishers, 1994
- 3) Armaly, B F , Durst, F , Pereira, J C F , and Schonung, B , "Experimental and Theoretical Investigation of Backward-Facing Step Flow", *Journal of Fluid Mechanics*, Vol 127, pp 473-496, 1983
- 4) Arnal M , and Friedrich, R , "Large-Eddy Simulation of a Turbulent Flow with Separation", In Turbulent Shear Flows VIII, ed. U Schumann, F Durst, B E Launder, F W Schmidt, J H Whitelaw, p 169 Berlin: Springer-Verlag
- 5) Bardina, J , Ferziger, J H , and Reynolds, W C , " Improved Subgrid Model for Large-Eddy Simulation", AIAA Paper, pp 80-1357, 1980
- 6) Ben-Artzi, M and Falcovitz, J , " A Second Order Godunov-Type Scheme for Compressible Fluid Dynamics", *Journal of Computational Physics*, No 55, pp.-1-32, 1984
- 7) Boersma, B J , Eggels, J G M , Pourquie, M J B M and Nieuwstdat, F T. M , "Large-Eddy Simulation Applied to an Electromagnetic Flowmeter", Proc Of the First ERCOFTAC Workshop on DNS and LES, Guildford, Surrey, U K , Kluwer Academic Publishers, 1994
- 8) Breuer, M , and Rodi, W., "Large-Eddy Simulation of Turbulent Flow Through a Straight Square Duct and 180° Bend," Proc. Of the First ERCOFTAC Workshop on DNS and LES, Guildford, Surrey, U K , Kluwer Academic Publishers, 1994
- 9) Bui, T T , "A Parallel Finite-Volume Algorithm for Large-Eddy Simulation of Turbulent Flows," NASA/TM-1999-206570, January 1999
- 10) Chakravarthy, S and Osher, S , "Numerical Experiments with the Osher Upwind Scheme for the Euler Equations," *AIAA Journal*, Vol 21, No 9, pp -1241-1248, 1983
- 11) Chakravarthy, S and Osher, S , "Upwind Schemes and Boundary Conditions with Applications to Euler Equations in General Geometries," *Journal of Computational Physics*, Vol 40, pp -447-481, 1983
- 12) Coirier, W J , " An Adaptively-Refined, Cartesian, Cell-Based Scheme for the Euler and Navier-Stokes Equations," NASA TM-106754, 1994

- 13) Colella, P and Woodward, P R , "The Piecewise Parabolic Method for Gas-Dynamical Simulations," *Journal of Computational Physics*, No 54, pp -174-201, 1984
- 14) Courant, R., Issacson, E , and Reeves, M " On the Solution of Nonlinear Hyperbolic Differential Equations by Finite Differences," *Comm Pure and Applied Mathematics*, Vol 5, pp 243-255, 1952
- 15) Dadone, A., Napolitano, M , "An Implicit Lambda Scheme," *AIAA Journal*, vol 21, No 10, pp -1391-1399, 1983
- 16) Deardorff, J W , " A Numerical Study of Three-Dimensional Turbulent Channel Flow at Large Reynolds Numbers," *Journal of Fluid Mechanics*, Vol 41, pp 453-480, 1970
- 17) Deiwert, G S , " Numerical Simulation of High Reynolds Number Transonic Flows," *AIAA Journal*, Vol. 13, No. 10, pp 1354-1359, 1975
- 18) Engquist, B., and Osher, S , " Stable and Entropy Satisfying Approximations for Transonic Flow Calculations," *Mathematics of Computation*, Vol 34, pp 45-75, 1980
- 19) Erlebacher, G , Hussaini, M Y , Speziale, C G , and Zang, T. A , "Towards the Large-Eddy Simulation of Compressible Turbulent Flows," *Journal of Fluid Mechanics*, Vol 238, pp 155-185, 1992
- 20) Germano M , "Differential Filters for the Large-Eddy Simulation of Turbulent Flows," *Physics of Fluids*, Vol. 29, pp 1755-1757, 1986
- 21) Germano M., "Turbulence, the Filtering Approach," *Journal of Fluid Mechanics*, Vol 238, pp 325-336, 1992.
- 22) Germano, M , Piomelli, U., Moin, P and Cabot, H , " A Dynamic Subgrid Scale Eddy Viscosity Model," *Physics of Fluids A*, Vol 3, July 1991, pp 1760-1765.
- 23) Ghosal, S , Lund, T S., Moin, P and Akselvoll, K , " A Dynamic Localization Model for Large-Eddy Simulation of Turbulent Flows," *Journal of Fluid Mechanics*, Vol 286, pp 229-255, 1995
- 24) Hakkinen, R. J., Greber, I , Trilling, L , and Abarbanel, S. S , " The interaction of an oblique shock wave with the laminar boundary layer," NASA Memo 2-18-59W, 1959.
- 25) Lesieur, M and Metais, O , " New Trends in Large-Eddy Simulations of Turbulence," *Annu Rev Fluid Mech.*, Vol 28, pp 45-82, 1996
- 26) Lilly, D. K., "A Proposed Modification of the Germano Subgrid-Scale Closure Method," *Physics of Fluids A 4 (3)*, pp 633-635, 1992

- 27) Lilly, D. K , "In Lecture Notes on Turbulence," ed JR Herring, JC McWilliams, pp 171-218 Singapore World Scientific 317 pp
- 28) Liou, M S and Steffen, C J, "A New Flux Splitting Scheme," *Journal of Computational Physics*, Vol 107, pp.-23-39, 1993
- 29) Manhart, M and Wengle, H , "Large-Eddy Simulation of Turbulent Boundary Layer Flow over a Hemisphere," Proc Of the First ERCOFTAC Workshop on DNS and LES, Guildford, Surrey, U K , Kluwer Academic Publishers, 1994
- 30) Moin, P , and Kim, J , " Numerical Investigation of the Turbulent Channel Flow," *Journal of Fluid Mechanics*, Vol 118, pp 341-377, 1982
- 31) Moin, P , Squires, K , Cabot, W and Lee S , "A Dynamic Subgrid -Scale Model for Compressible Turbulence and Scalar Transport," *Physics of Fluids A*, Vol 3, pp 2746-2757, 1991.
- 32) Moretti, G , " The  $\lambda$ -schemé," *Computers and Fluids*, Vol 7, pp 191-205, 1979
- 33) Muralidhar, K , and Sundarajan, T , Computational Fluid Flow and Head Transfer, Narosa Publishing House, New Delhi, India, 1995
- 34) Napolitano, M and Dadone, A , "Implicit Lambda Methods for Three-Dimensional Compressible Flow," *AIAA Journal*, Vol 23, No 9, pp -1343-1347, 1985
- 35) Roe, P. L., "Approximate Riemann solvers, Parameter Vectors and Difference Schemes," *Journal of Computational Physics*, Vol 43, pp 357-372, 1981
- 36) Sagaut, P , Troff, B , Le, T H , and Loc, T , P , "Two-dimensional Simulations with Subgrid Scale Models for Separated Flow," Proc Of the First ERCOFTAC Workshop on DNS and LES, Guildford, Surrey, U K , Kluwer Academic Publishers, 1994
- 37) Sarkar, S , "Numerical Simulation of Supersonic Slot Injection Into A Turbulent Supersonic Stream," *International Journal of Turbo and Jet Engines*, Vol 17, pp -227-240, 2000
- 38) Schumann, U , "Subgrid Scale Model for Finite-Difference Simulations of Turbulent Flows in Plane Channels and Annuli," *Journal of Computational Physics*, Vol 18, pp 376-404, 1975
- 39) Sengupta, T K , and Nair, M T , " Upwind Schemes and Large Eddy Simulation," *Int J Numer Meth Fluids*, Vol 31, pp 879-889, 1999
- 40) Driver and Sigmiller, Backward Facing Step with Inclined Opposite Wall, Experimental Data, 1995

- 41) Smagorinsky, J., "General Circulation Experiments with the primitive Equations, *Monthly Weather Review*, Vol 91, pp 99 -164, 1963.
- 42) Squires, K D , "Dynamic Subgrid-Scale Modeling of Compressible Turbulence," Annual Research Briefs, Stanford University Center for Turbulence Research, Dec 1991, pp 207-223
- 43) Steger, J L., Warming, R. F , "Flux Vector Splitting of the Inviscid Gasdynamic Equations with Application to Finite-Difference Methods," *Journal of Computational Physics*, No 40, pp -263-293, 1981
- 44) Thomas, T G , Williams, J J. R , "Large-Eddy Simulation of compound channel flow with one floodplain at  $Re \approx 42000$ ," Proc Of the First ERCOFTAC Workshop on DNS and LES, Guildford, Surrey, U K , Kluwer Academic Publishers, 1994
- 45) Van Leer, B , " Towards the Ultimate Conservative Difference Scheme IV A New Approach to Numerical Convection," *Journal of Computational Physics*, Vol 23, pp 276-299, 1977
- 46) Vreman, B, Geurts, B. and Kuetren, H , "Large-eddy simulation of the turbulent mixing layer," *Journal of Fluid Mechanics*, Vol 339, pp -357-390, 1997
- 47) Vreman, B, Geurts, B and Kuetren, H , "Subgrid Modeling in LES of Compressible Flow," Proc Of the First ERCOFTAC Workshop on DNS and LES, Guildford, Surrey, U K , Kluwer Academic Publishers, 1994
- 48) Warming, R F., Beam, R M , "Upwind Second-Order Difference Schemes and Applications in Aerodynamic Flows," *AIAA Journal*, vol 14, No 9, pp.-1241-1249, 1976
- 49) Yoshizawa, A., "Statistical theory for compressible turbulent shear flows, with the application to the subgrid modeling," *Physics of Fluids A*, Vol 29, pp -2152-2164, 1988

133643

133643  
Date Slip

The book is to be returned on  
the date last stamped



A133643

A133643

TH

ME/2001/M

G346C